Cosmic ray efficiency studies for the Radio Neutrino Observatory Greenland (RNO-G)

Bachelorarbeit aus der Physik

Vorgelegt von

Robin Valk

08.01.2024

Erlangen Centre for Astroparticle Physics (ECAP)

Friedrich-Alexander-Universität Erlangen-Nürnberg

Betreuer: Prof. Dr. Anna Nelles

Abstract

The detection of ultra high energy cosmic rays ($E > 10^{16}\,\mathrm{eV}$) at the Radio Neutrino Observatory Greenland (RNO-G) uses a triangular configuration of upward facing logarithmic dipole antennas (LPDA) at each station. The main focus of this study is a comparative analysis of the trigger efficiency provided by a triangular and a quadratic surface antenna configuration, and to evaluate both in terms of directional consistency in azimuth. The surface trigger efficiency for cosmic ray induced air showers is obtained through simulations based on the hardware responses of station layouts, and on simulations of air showers using a Monte Carlo based approach and the implementation of endpoint formalism to calculate the generated radio signals. In the scope of this thesis, it will be conclusively demonstrated that the quadratic configuration outperforms the triangular configuration. The station layout with 4 surface trigger channels has only 4 lows in detection rate over the entire 360 deg azimuth range, while the 3 surface trigger channels have 6 Blindspots. The results of the simulations yield, that the 4 antenna layout performs 37.0 % better in terms of total detection rate, and has a 53.0 % smaller relative deviation in azimuth.

Contents

List of Figures

1 Introduction

Neutrinos are ideal messangers of astronomical events, as they can pass freely through space and are unlikely to interact with stellar dust, and they remain relatively unaffected by gravitational wells. However they are very hard to detect for the very same reasons.
The Radio Neutrino Observatory Greenland (RNO-G) is built for measuring the interaction of ultra high energy (UHE) neutrinos within the glacial ice sheets covering Greenland. However, when ultra high energy cosmic rays (UHECR) interact with the atmosphere and cause an air shower, ultra relativistic muons are produced in one of the decay channels, that can penetrate the ice as well and cause a signal similiar to a neutrino interaction. Therefore, RNO-G needs a sufficient trigger efficiency for cosmic ray (CR) events. For this purpose, the RNO-G stations already deployed in the field have been built using a triangular arrangement of upward facing surface antennas sensitive to air shower signals. The main focus of this study is to determine whether 4 upward facing antennas in a quadratic configuration would offer a better chance at triggering air shower induced radio pulses averaged over the possible spectrum of CR arrival directions, and to compare which performs less consistent over the possible range of arrival directions. Since both configurations lie flat in the azimuth plane, comparing the respective trigger efficiencies as functions of azimuth is of special interest.
To answer this question, extensive simulations based on the hardware responses of the two design options were conducted, for air showers in an ultra high energy range of $[10^{16}, 10^{18.5}]$ eV, and for a sufficiently large enough range of possible arrival directions, so that the respective trigger efficiencies for cosmic ray events could be formulated as a function of arrival direction.
In chapter 3, an overview of the signal chain and the hardware responses are given. In chapter 4, the Monte Carlo based approach of simulating extensive air showers and their radio pulses is explained shortly, as well as the procedure used to simulate the trigger decisions for each configuration. Following this, to determine possible blindspots, a comparative evaluation of the overall performance level of the triangular and the quadratic antenna configuration is given in chapter 5, with special focus on the consistency of performance over the range of arrival azimuth.

2 Theoretical Background

The following section will give an overview of the challenges associated with neutrino detection, and the resulting building considerations and demands that shaped the design of RNO-G. Furtermore, the basic development of a particle cascade, both in dense medium and in the atmosphere will be explained shortly, as well as the emission meachanisms responsible for the produced radio signals.

2.1 Concept of RNO-G

When an ultra high energy (UHE) neutrino, above PeV energies (10^{15} eV), collides with a nucleus in dense medium, the induced particle cascade produces a measurable radio pulse. The Radio Neutrino Observatory Greenland (RNO-G) is built for measuring these radio pulses. Because of their low interaction crosssection, the chance of a neutrino interacting with the medium are only sufficiently high enough if the medium is dense enough and if the energy of the neutrino is large enough, as this decreases their interaction length. The solid crust of the earth only becomes opaque to neutrinos above the PeV threshold [1].
Furthermore, in dense media there is a high reaction chance for most particle types produced by the primary and subsequent interactions, so the main body of a cascade only unfolds over a few meters, before the average particle energy falls below the interaction threshold. On top of this, the extremely energetic neutrinos RNO-G aims to detect, are exceedingly rare at the energies in question and above. Because of these reasons, for a reasonable chance of detection, a potential detector needs to survey a very large volume of an appropriate interaction medium, at an appropriate location. An appropriate choice of location for the detector demands distance from civilisation, so that the considerable radio noise produced by humans doesn't drown the potential radio pulses. An appropriate choice of medium demands that the propagation of the cascade in the medium is well understood, as well as the emission mechanism of the radio pulse, and that the medium is transparent to radio waves. These conditions are met by large sheets of

Figure 1: Location of summit station in Greenland, marked with blue star. Figure adapted from [15].

Figure 2: Antenna deployment. Surface antennas deployed in shallow trenches, deep antennas lowered into boreholes. Figure adapted from [16]

ice, which were recommended as a detection medium by G. Askaryan in 1965 [4], and which has been demonstrated successfully by previous experiments conducted on large volumes of radio transparent ice, like the IceCube experiment in Antarctica [13].
Because the attenuation lenght of radio waves is multiple kilometers in ice, one can cover the large volumes required with large spacing between the antennas inserted into the ice sheet, making radio detection of particle cascades in ice relatively cost efficient [3]. This makes the glacial ice sheets covering Greenland an ideal choice. The Radio Neutrino Observatory Greenland shows the first large scale implementation of this technology: 35 stations as shown in figure 4 will be constructed on roughly $40\,\mathrm{km}^2$ at summit station. Up until 2022, 7 stations have already been deployed.

With each addition to the observed volume, the chance of detection increases. Therfore, even a single detection or non detection in the observed volume of medium, will give much sought constaints on the astronomical neutrino flux beyond the previously observed energy range [3]. There is a continous development of software tools to improve the reconstruction chain from

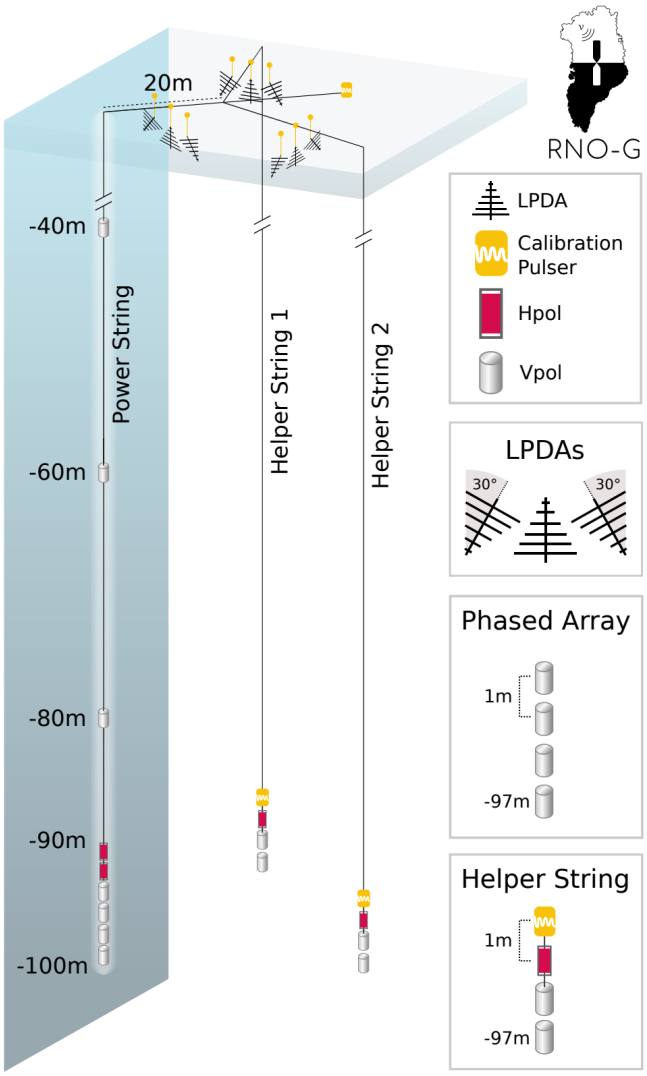

Figure 3: Design of a RNO-G single station, with logarithmic periodic dipole antennas (LDPA's) deployed in shallow trenches at surface level, and Vpol and Hpol antennas installed in deep boreholes. The 9 surface LDPAs are sensitive to air shower induced radio pulses, especially the 3 upward facing antennas, while the 6 downwards angled ones have a higher sensitivity to radio pulses induced by cascades in the ice. The vertical polarized (Vpol) and horizontal polarized (Hpol) antennas also serve the purpose of detecting radio pulses produced below ground. Figure adapted from [16].

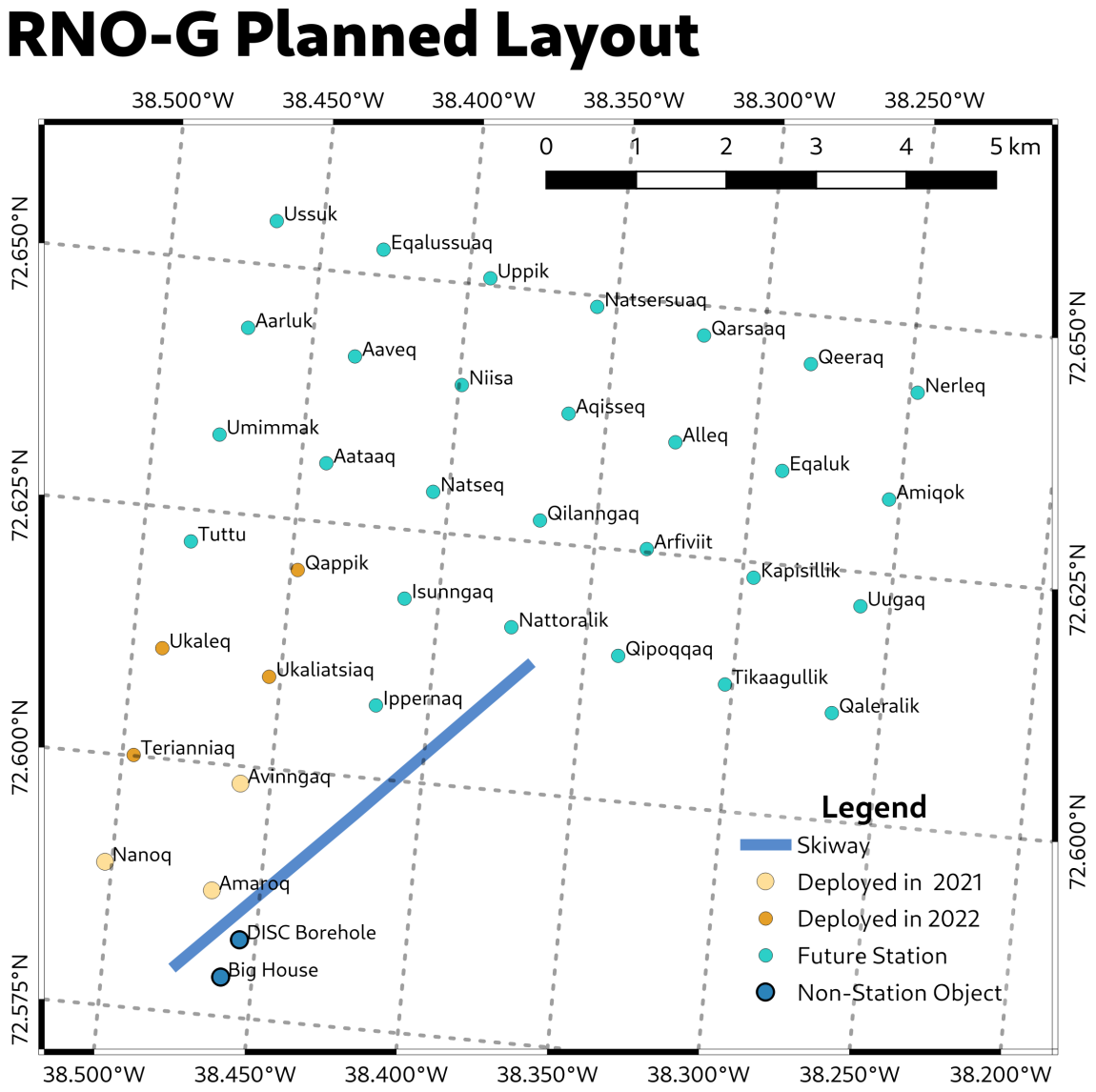

Notes:

- Station numbering follows a grid, where the first numeral is in increasing W-E and the second numeral is in increasing S-N, skipping non-existent stations (the Seckel method).
- Station spacing is 1.25 km in map coordinates (but really 1.23 km due to projection, which creates a 2% scale difference.)
- Projection is Greenland Polar Stereographic (EPSG:5938). True north indicated by Rose, offset from grid north by 5.37°.
- Magnetic Declination, for August 1 2022, is -25.2° according to the WMM.
- In list below, all future stations labeled as 2023.

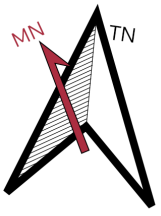

v 0.5.1
2022-08-26
68000:1
Greenland Polar Stereographic Projection (EPSG:5938)

Figure 4: Layout of planned RNO-G stations. Figure produced by the RNO-G Collaboration [2].

detection, emission, and propagation of particle cascade, so that with the data collected the origin and energy of the primary can be reconstructed with good confidence. Additionally, RNO-G will test technology that is of immediate relevance for the radio array of IceCube-Gen2, which is to be built at South Pole as a successor to IceCube.[1].

2.2 Radio detection of Neutrinos

The reaction paths available to a neutrino when it collides with one of the nucleons, either a proton or a neutron, of a nucleus of the ice, are limited to weak interaction, and therefore to the exchange of either a charged $W^{\pm}$ or a neutral Z^0 boson. The primary interaction is therefore classified as either a charged-current (CC) or a neutral-current (NC) interaction. The fundamental symmetries and laws of conservation restrict the possible outcomes of these interactions. Both CC or NC interactions will produce one or multiple hadrons, mostly pions ($\pi^0, \pi^{\pm}$), as well as some protons, neutrons and kaons [19]. Because both charge and lepton count are conserved in weak interactions, a CC interaction of a neutrino ν_l with a proton or neutron has to produce a charged lepton $l \in \{e^{\pm}, \mu^{\pm}, \tau^{\pm}\}$, besides the hadronic products:

$$\nu_l + \text{nucleon} \xrightarrow{\text{CC}} l + \text{hadron(s)}\,, \tag{2.1}$$

while a NC interaction will produce another neutrino for the very same reasons:

$$\nu_l + \text{nucleon} \xrightarrow{\text{NC}} \nu_l + \text{hadron(s)}. \tag{2.2}$$

Because the ice becomes transparent to neutrinos below the PeV limit, the neutrino produced from a NC interaction will not react again.
The free protons and neutrons and the charged pions $\pi^{\pm}$ build the hadronic component of the cascade. Because they posses very great energy, their decay length $l_{\text{decay}} = \gamma \cdot 7.8\,m$ [15], with γ here as the relativisitc gamma factor, remains larger than their interaction length for a number of interactions, despite the fact that the hadronic interaction is mediated through the short-ranged strong force. Therefore they will continue to interact with nuclei of the medium, producing more pions. The reactions cease once the decay length becomes shorter than the interation length, and the charged pions will decay, mostly into muons ($\pi_{\pm} \longrightarrow \mu^{\pm} + \overset{(-)}{\nu}_{\mu}$). The neutral pions have a very short decay length of $l_{\text{decay}} = \gamma{\cdot}2.5{\cdot}10^{-8}\,\text{m}$ [15], with γ again here as the relativisitc gamma factor, and therefore most will decay into a photon pair ($\pi^0 \longrightarrow \gamma{+}\gamma$), which will build the electromagnetic component of the cascade. The dominant processes that build

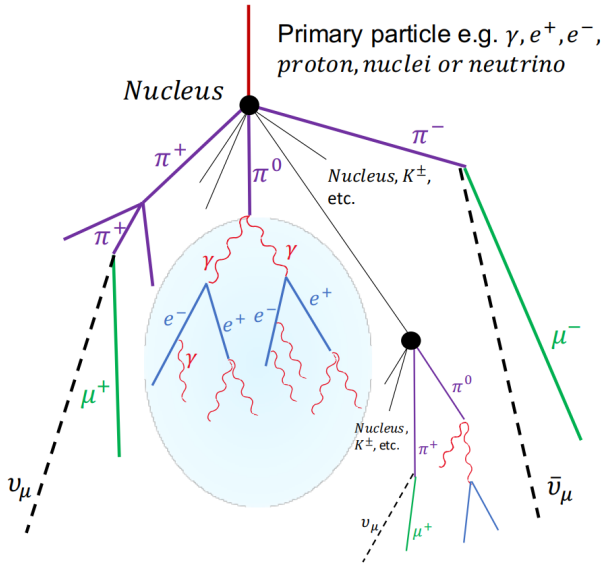

Figure 5: Most important interaction branches and decay channels in a particle cascade. Figure taken from [15].

the electromagnetic component are the emission of photons by Bremsstrahlung ($e^\pm \longrightarrow e^\pm + \gamma$) and the production of electron-positron-pairs by photons ($\gamma \longrightarrow e^- + e^+$). Coulomb scattering and ionisization of the medium produce more electrons and photons as well, which further adds to the electromagnetic component. The created electrons, positron and photons continue to interact and build, until the average particle energy falls below the ionization energy of the medium [19].

If a CC primary interaction is of an electron neutrino ($\overset{(-)}{\nu}_e + \text{nucleon} \xrightarrow{\text{CC}} e^\pm + \text{hadron(s)}$), either an electron or a positron is produced, which creates an electromagnetic shower immediately. However, this is not the case if the primary interaction is of a muon or tauon neutrino, as the produced muon or a tauon, can travel several kilometers through the ice until they decay, creating multiple subshowers in the process [7].

The mechanism responsible for the radio pulse produced by the electromagnetic component is called the Askaryan effect [4]. Because the electromagnetic component interacts with the medium, ionizing its atoms, leaving positively charged ions behind and dragging the free electrons along, an excess of negative charged particles forms at the front of the shower. Because the medium is dense, there are many instances of ionization and scattering, and the charge excess that builds up over time becomes quite strong. This varying of the net charge over time induces linearly polarized radiation, with the polarization being oriented in the direction of the so called shower axis $\vec{v}$, also the incoming direction of the primary neutrino, as the charge asymmetry is aliged along the propagation of the cascade, as can be seen in figure 6.

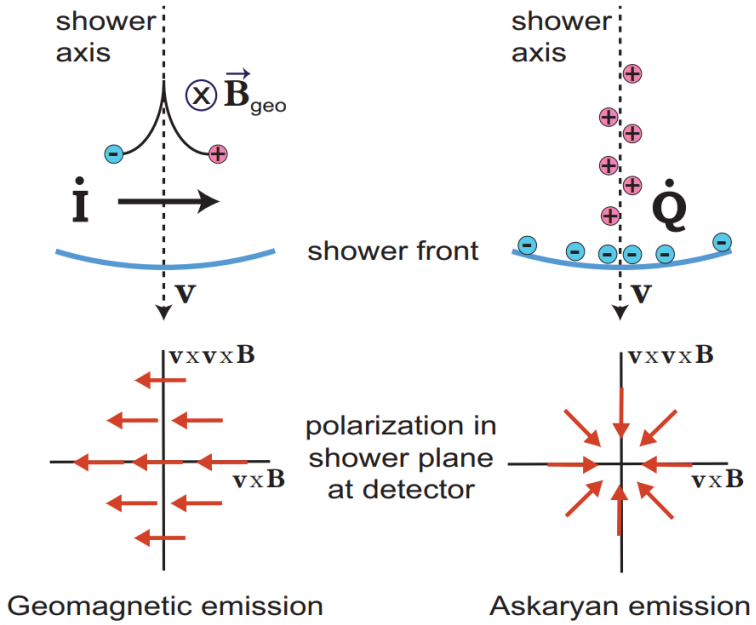

Figure 6: Polarization of geomagnetic and askaryan radio emission, figure taken from [18].

An important effect that depends on the medium is the so called Cherenkov compression. Because the particle cascade moves at relativistic speeds, it can move slightly faster than the speed of light in the medium, and propagate faster than the emitted radio signals in the medium. This compresses the duration of the emission observed at a distance in time, while it enhances the intensity of the pulse. This enhancement peaks at a certain observing angle, which is called the Cherenkov-angle:

$$\cos\theta_c = \frac{1}{n \cdot \beta}\,, \tag{2.3}$$

which depends on the refractive index of the medium n, and the relativistic velocity $\beta = \frac{v}{c}$ of the source of emission. With the refractive index of ice $n_{\text{ice}} \approx 1.78$, this leads to a cherenkov angle of $\theta_c^{\text{ice}} \approx 56$ deg [15]. Observing the radio pulse from the so called Cherenkov cone, observing at the cherenkov angle to the shower axis $\vec{v}$ like depicted in figure 7, leads to maximum signal strenght and coherency [4]. The radio pulse from a particle cascade in ice is only strong enough to trigger the detector, when observed in the cherenkov cone [3].
For the radio detection of particle cascades in the ice, an RNO-G station deploys downward facing antennas at the surface, as well as antennas lowered into deep boreholes, as depicted in figure 7.

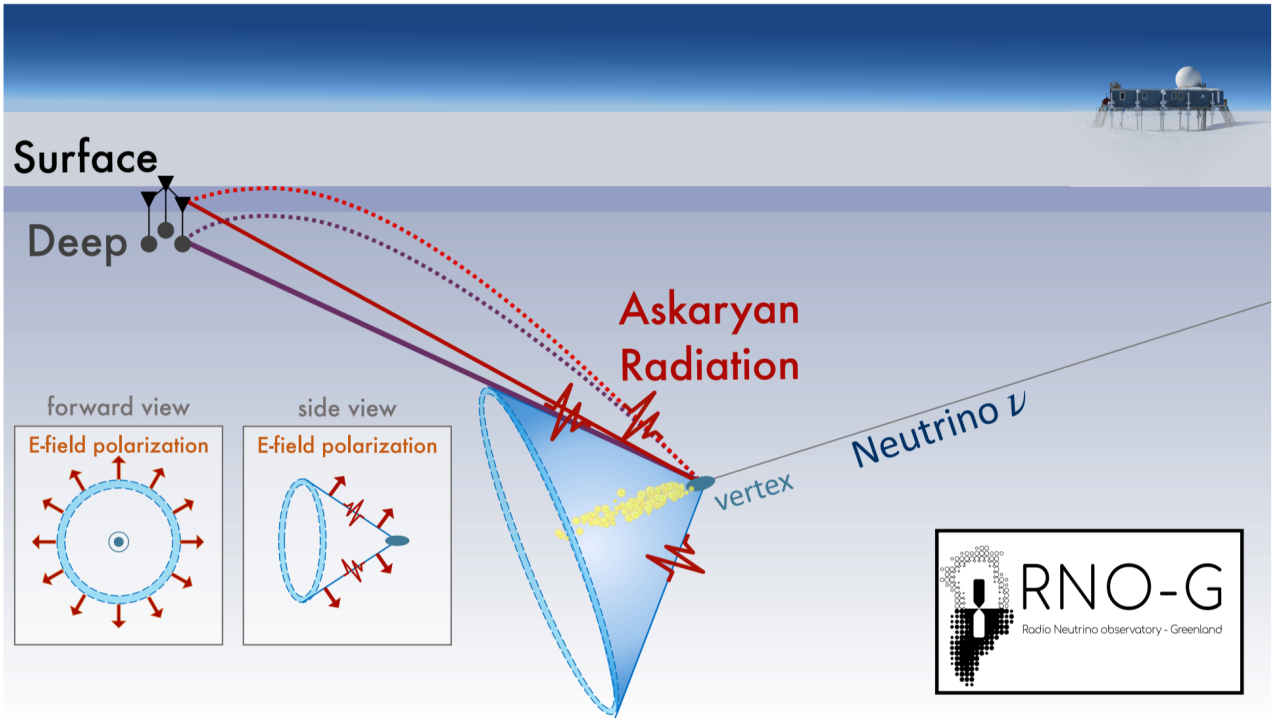

Figure 7: Visulaisation of the Cherenkov cone for a neutrino induced particle cascade below ice. Figure produced by the RNO-G Collaboration [3].

2.3 Radio detection of Cosmic Rays

The phenomena of extensive air showers was discovered in 1938 by Pierre Victor Auger, and it predates the theory of particle showers in dense medium. An air shower can be caused by any primary particle, as long as it has enough energy to set off a hadronic particle cascade, as described in the previous section. Typical cosmic ray primaries are protons, neutrons or larger nuclei such as iron, but an air shower could also be caused by photons, electrons or neutrinos [19]. Unlike neutrinos however, electrons, photons or hadronic primaries, have a reasonable chance of interaction with the atmosphere. The hadronic particle cascade unfolds as described in the previous section and depicted in figure 8, with the hadrons produced from the strong hadronic interactions mostly being pions, with the neutral pions quickly decaying into a photon pair, that cause the electromagnetic cascade of photons, electrons and positrons, and the charged pions continuing to interact with the medium, which produces mostly pions again, and adding to the hadronic component of the particle shower, until their relativistic speed becomes too slow to pass through enough medium to have a reasonable chance of interaction before decaying. Because the molecules of the atmosphere are spread much more thinly than the ice molecules, the traveling particles of the cascade have a greater interaction length than in

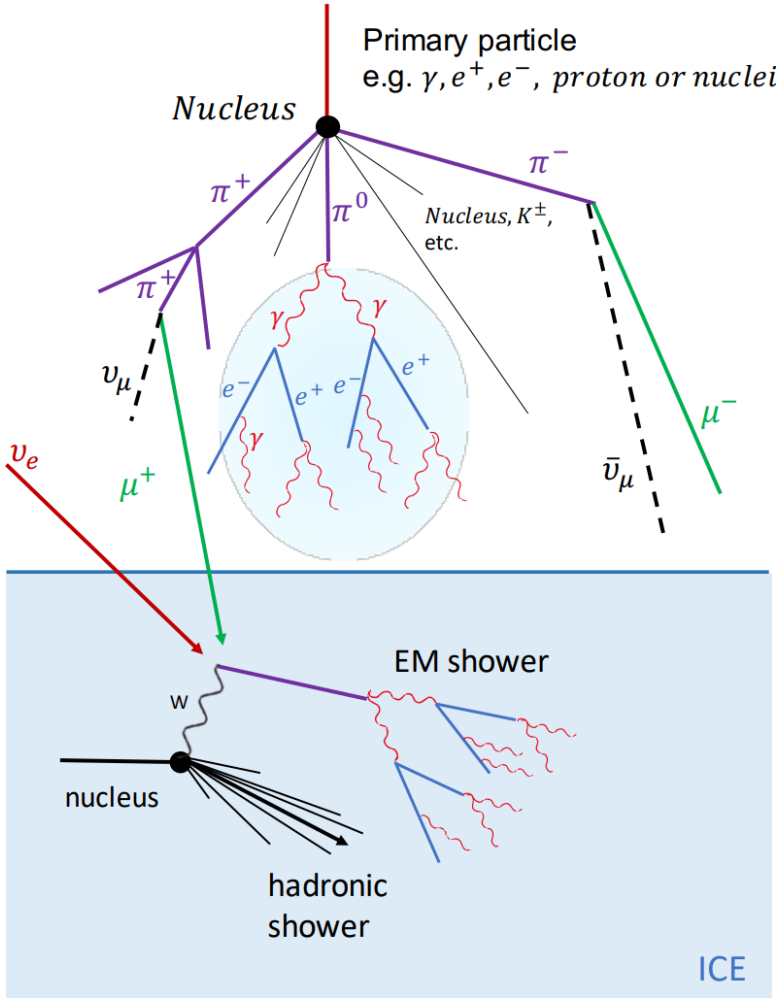

Figure 8: Visualization of an air shower and a particle cascade produced by an electron neutrino below ice. Atmospheric muons that are produced commonly in an air shower can induce an electromagnetic cascade in the ice similar to a neutrino induced cascade. Figure taken from [15]

the denser ice. Therefore an air shower develops over a range of kilometers, whereas particle showers in dense medium develop over a range of meters [19]. When the charged pions decay into muons ($\pi^\pm \longrightarrow \mu^\pm + \overset{(-)}{\nu}_\mu$), enough energy is transmitted to the produced muon, so that it is able to reach the ground at highly relativistic speeds, despite having a much shorter decay length than the distance to the ground, and it is able to cause an electromagnetic cascade below ground, once it decays into an electron ($\mu^\pm \longrightarrow e^\pm + \overset{(-)}{\nu}_e + \overset{(-)}{\nu}_\mu$), which is visualised in figure 8. Atmospherically produced muons produced by air showers are a well understood phenomena, and they were first detected in 1936 by Carl D. Anderson and Seth Neddermeyer.
RNO-G requires a sufficent detection efficiency of air showers, so that in the case of a potential neutrino interaction in the ice, causing an electromagnetic cascade that triggers the below

ground antennae, it becomes certain whether an atmospheric muon can be excluded as an alternative origin for the signal.

The theoretical basis of radiation produced by air shower was developed by F.D. Kahn and I. Lercke in 1965 [12]. While the Askaryan effect is also responsible for parts of the radio pulse produced by an air shower, it plays a much lesser role than for cascades in denser medium, as the effects leading to the charge asymmetry are dependend on the electromagnetic component interacting with the medium. An air shower's radio emission is mostly the product of another effect called geomagnetic radiation, and as the name hints it is the result of the shower interacting with the earths magnetic field [17]. Whereas in dense media, geomagnetic emission becomes completely negligable in contrast to Askaryan emission, for a particle shower in the atmosphere, it becomes the dominant emission mechanism.

The electrons and positrons that make up the electromagnetic component of the shower, are accelerated by the Lorentz force $\vec{F}_B \propto \vec{v} \times \vec{B}$, as they move along the shower axis $\vec{v}$ at an angle to Earth's magnetic field $\vec{B}$. This results in a current $\dot{I}$ flowing along the $\vec{v} \times \vec{B}$ axis, which varies over time, as the amount and distribution of electrons and positrons changes with the evolution of the shower. The deflection of the charged particles in the magnetic field results in the emission of radio waves, that are linearly polarized along the $\vec{v} \times \vec{B}$ axis, which is shown graphically in figure 6.

Again, cherenkov compression plays an important role for detection, as it improves signal amplitude and coherency [12]. The refractive index of the atmosphere is a gradient of hight over sea level $n(z)$, that is 1.0003 at sea level and becomes 1 as the air thins at greater hights, which results in a Cherenkov angle of $\theta_c^{\text{air}} \approx 1\,\text{deg}$ for air shower induced radio pulses [3]. While the cherenkov compression is less significant than in dense medium, the signal intensity and coherence still drops signifcantly outside the cherenkov cone, which becomes visible in the shower patterns shown in figure 9.

For the detection of an air shower induced radio pulse, each RNO-G station is equipped with upward facing surface antennas, as shown in figure 3.

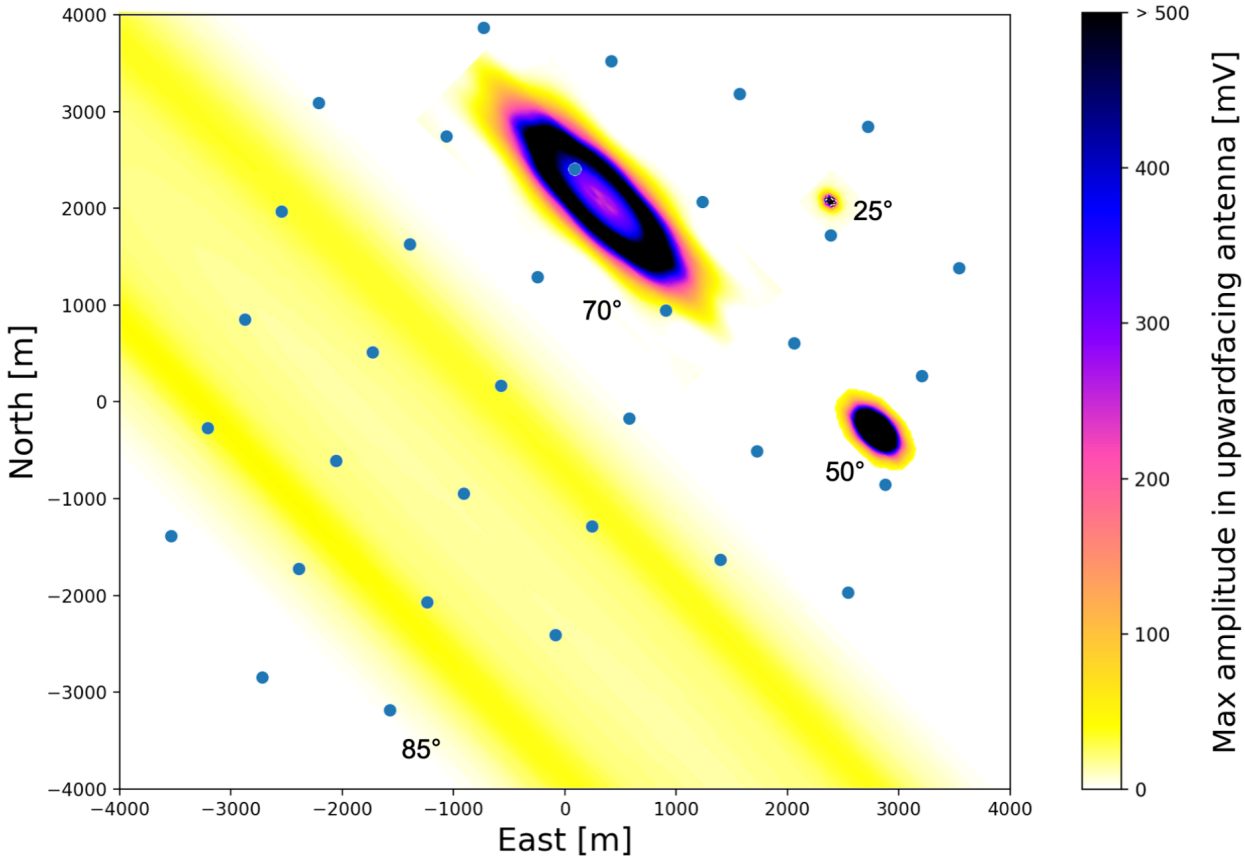

Figure 9: Simulated footprint of an air shower induced radio pulse at primary energy $E = 10^{18.5}\,\mathrm{eV}$, at arrival azimuth $\phi = 0$ and different arrival zeniths. The maximum amplitude of the upward facing surface channels as a function of location on the ground plane is used for visualization of the footprint. The signature shape of the cherenkov cone becomes visible for greater arrival zeniths. Figure taken from [3].

3 Trigger strategy for air showers at RNO-G

The concept of RNO-G entails continous surveillance of a large volume of medium, over long periods of time. However, the continous recording of all channel feeds would quickly build up a tremendous amount of data. Moreover, an indication is needed at what time an actual event might have been recorded, and what parts of the feed are actual data worth analysing. Therefore, an efficient trigger strategy is needed, both for air showers and signals originating from within the ice. The following segment will outline the signal chain for triggering an air shower signal.

3.1 Signal chain

The surface LPDA's are sensitive to electromagnetic radiation in a range of 105 MHz to 1300 MHz [15]. In figure 11, the simulated signal response of an upright standing LPDA antenna facing North, to the simulated radio pulse produced by an air shower initiated by a cosmic ray event is shown. The incident energy was $E = 10^{18}\,\mathrm{eV}$, arriving at zenith $\theta = 55$ deg and at azimuth $\phi = 0$. In the so called SURFACE board, oscillations of voltage in an antenna, which mirrors oscillations of the electric field polarized along the length of the antenna, are amplified and filtered outside a frequency band of 80 to 700 MHz. The SURFACE board was specifically designed for the requirements of RNO-G, to surpress the galactic noise below the $\sim 80\,\mathrm{MHz}$ range, and to accomodate for the wireless data transmission using LTE technology at $\sim 880\,\mathrm{MHz}$ [15], as can be seen in figure 12. After amplification, the channel output is transmitted via coax cable to an analog to digital (ADC) converter, which stores a short history of the digitalised recordings, as well as to the surface trigger. The surface trigger processes the channel feed further and checks for the trigger conditions. If the requirements are met, the

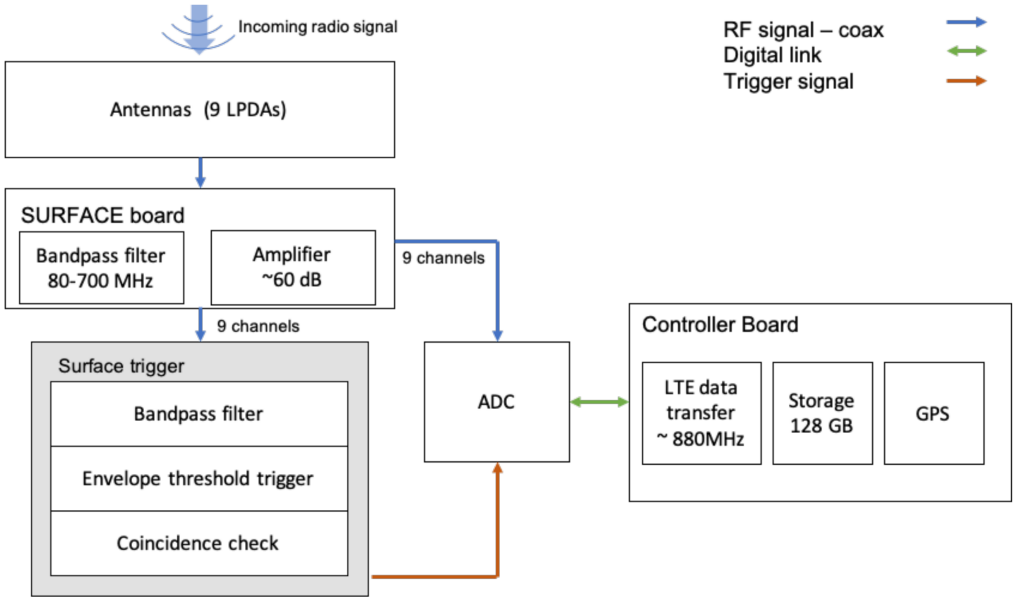

Figure 10: Visualization of the surface channel signal chain for triggering an air shower event. The signal response of the surface antennas is amplified and filtered outside the 80 to 700 MHz. The channel feeds are then passed on to an analog to digital (ADC) converter, which stores a short history of the digitalised recordings, as well as to the surface trigger. If the input fulfills the trigger requirements, the surface trigger signals the ADC converter to transmit the digitalized channel feeds for a time intervall around the time of triggering. The data is then transmitted to the controller board wirelessly. Figure taken from [15].

digitalized data is then transmitted in a time window around the trigger event to the controller board. A visualization of the signal chain is presented in figure 10.

3.2 Trigger Conditions

The surface trigger has been optimized for triggering the atmospheric radio pulse produced from an air shower. The signal responses from the 3 upward facing LDPA's are chosen as trigger channels and spikes in the signal strength above a certain voltage threshold will result in triggering. To minimize the chances of spikes in the radio background causing an accidental triggering, several other criteria have been optimized to accomodate for the various different noise sources. A source of constant noise, that is seen coherently by every channel, is the diffuse radio emission of the galaxy. Since the location of RNO-G is relatively close to earths rotational axis, the area of the radio sky seen by it changes very little, so there is little fluctuation over the course of a day. The bandpass filter of the SURFACE board has been chosen specfically to

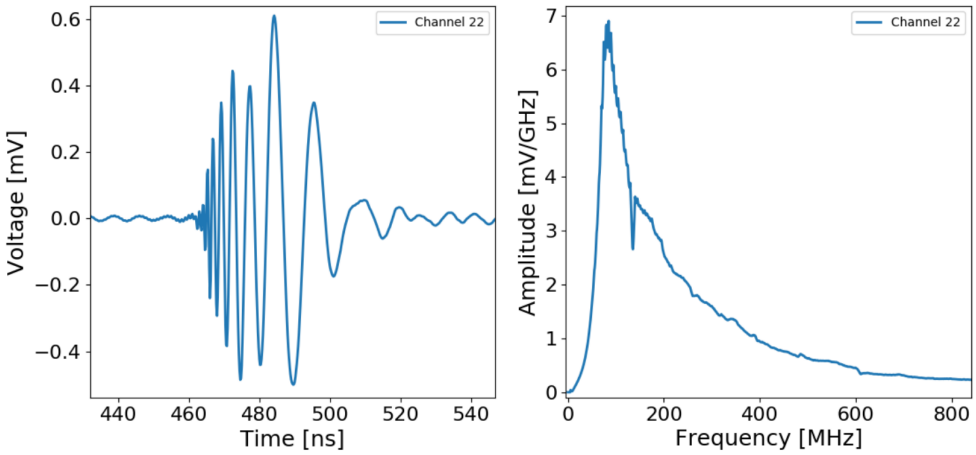

Figure 11: Simulated induced antenna voltage by the electric field generated by an air shower, for a primary energy of $E = 10^{18}$ eV, arriving at zenith $\theta = 55$ deg and at azimuth $\phi = 0$. The LDPA is oriented upwards and rotated facing north. The antenna response is shown without amplification, on the left as a function of time, on the right as a function of frequency. Figure taken from [15].

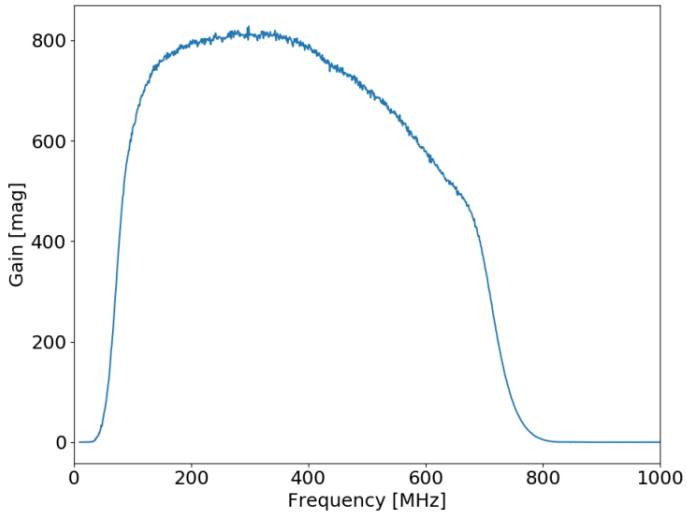

Figure 12: SURFACE board amplification and filtering, signal gain as a function of frequency. Figure taken from [15].

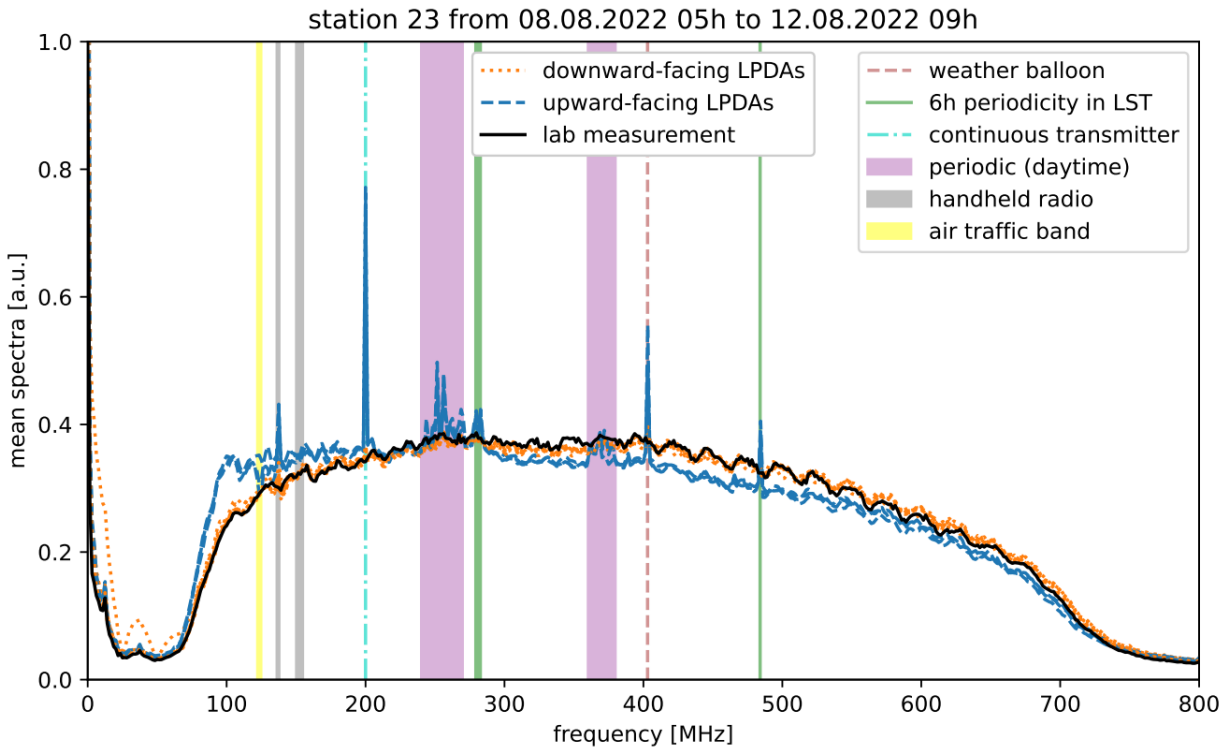

Figure 13: Radio background recorded by a RNO-G single station over the course of 4 days. In blue, the spectrum seen by the upward facing LPDA's. The vertical lines denote various narrow and broadband sources of known radio noise. Figure taken from [16].

filter out it's most significant bandwidth. Radio sources of human origin, like air traffic passing through the area or the weather ballon that takes of regularly from summit station, have to be communicated taken into account accordingly [16]. An example of the radio background seen by the LPDA's over the course of one day is shown in figure 13. The most significant and constant source of noise is thermal noise, which is the only fluctuation to the signal strenght that affects each channel incoherently and at random. Therefore, to allow for a lower trigger channel voltage threshold and better detection sensitivity, while keeping the chance of a random thermal noise spike triggering low, of the three trigger channels, a two channel coincidence has to be met in a 50 ns coincidence window to successfully trigger an event. As can be seen from figure 13, the radio background recorded by a RNO-G station, averged over the course of 4 days, is constant in strength over the observerd frequency range, and mirrors the amplification curve of the SURFACE board component seen in figure 12. Comparing this with the radio pulse to be expected from an air shower, which is stronger in the lower frequency range of the passband, as can be seen in figure 11, it makes sense to introduce an additional passband

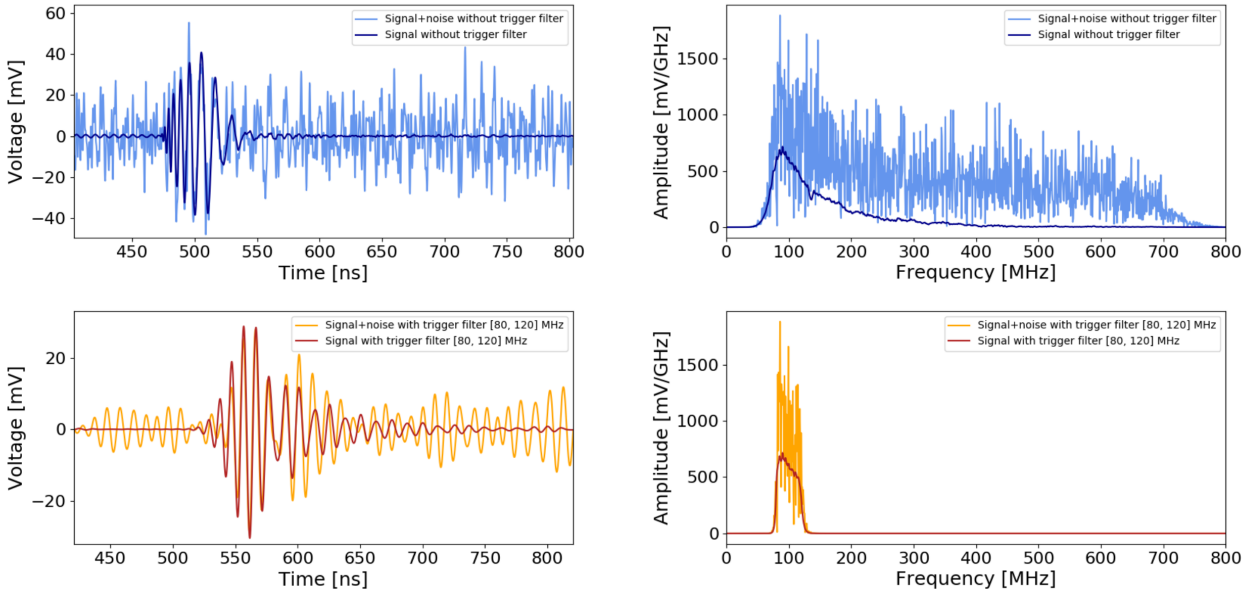

Figure 14: Example of bandpass filter applied to the trigger signal. On the top, in blue, the amplified channel feed is shown without additional filtering. In light blue, the same signal is shown against a simulated thermal and galactic noise background. On the bottom, in red, the amplified channel feed is shown with a $[80, 120]$, MHz bandpass filter, in orange with simulated noise. On the left in the time domain, on the right in the frequency domain, for both respectively. Because the signal strength decreases significantly for higher frequencies, while the noise does not, the channel response stands out more clearly against the noise background in the lower frequncy range, which is why a trigger decision based on a lower frequency passband is less ambiguous. Figure taken from [15].

filter to the trigger signals, in a frequency range where the expected signal from an air shower is distinguished most against the background. Figure 14 shows that the inclusion of such a filter can deliver on this. The signal of a trigger channel breaching the trigger threshold can be simulated by applying a hilbert transformation to the trigger channel output [15], which yields the hilbert envelope of the signal function as seen in figure 15. The best combination of the bandpass range for the trigger signal, the duration of the coincidence window and the trigger threshold voltage, has been analysed extensively in the scope of a study on optimizing the triggering strategy for the detcetion of cosmic rays at RNO-G by Lilly Pyras. Most of the figures used in this chapter for the explantion of the signal chain and the triggering strategy originate from her thesis [15].

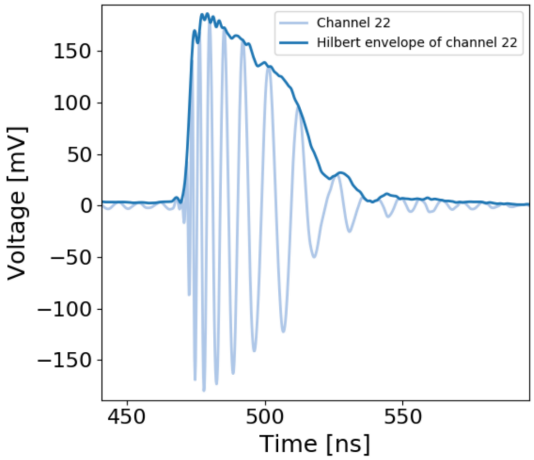

Figure 15: Hilbert enveloped channel response. If the maximum of this function surpasses the trigger threshold, the channel triggers. Figure taken from [15].

4 Simulations

In the scope of a study on optimizing the triggering strategy for the detcetion of cosmic rays at RNO-G by Lilly Pyras [15], a set of 407 air showers was simulated using a Monte Carlo approach. The method generates numeric results by repeatedly sampling the stochastics of the interaction crosssections and decay propabilities of single particles. The simulation files were originially provided by Prof. Dr. Christian Glasser. In the following, the process of simulating the evolution of one such particle shower and the radio signal emissioned by it is explained shorty. Afterwards, the simulations conducted with this set on the two different detector layouts for the scope of this study are adressed.

4.1 Air shower simulations

The simulations were run with the software "CORSIKA 7.6400" [9], assuming protons as primaries, and hadronic interaction models QGSJetII.04 [14] and UrQMD [5]. Atmosphere and magnetic field match conditions at summit station in 2020.
The CORSIKA programm allows for the tracking of particles through the atmosphere, as well as the tracking of subsequent decay branches and air nuclei reaction products. All decay branches down to the 1% level are taken into account. It can run simulations for different primary particles, such as protons and iron atoms, and allows for implementation of different hadronic interaction models, which determine stochastics and crosssections of the hadronic component's decay and interaction branches [9].
While CORSIKA provides the position, time and energy of each tracked particle at the start- and endpoint of individual track segments, an extension called CoREAS can use these to calculate the radio emissions produced by the deflection of charged particles in the earths magnetic field with the endpoint formalism [10]. The endpoint formalism is a method of numerically calculating the electromagentic radiation produced by charged particles along their path of acceleration, and it "relies on the fact that any trajectory of a charged particle undergoing

acceleration can be decomposed into a series of discrete 'acceleration events', joined by straight tracks" [11]. By dissecting the particle trajectories into enough track segments, and by stacking the endpoint emissions, an air showers combined radio emission can be simulated. The electric field component of the electromagnetic radiation emitted by such an individual endpoint, as it is observed at a point $\vec{x}$ and at frequency ν, is calculated as:

$$\vec{E}_{\pm}(\vec{x},\nu) = \pm\frac{q}{c}\frac{e^{ikR(t_0')}}{R(t_0')}\frac{e^{2\pi i\nu t_0'}}{1-n\vec{\beta}^*\cdot\hat{r}}\cdot\hat{r}\times\left[\hat{r}\times\vec{\beta}^*\right], \tag{4.1}$$

where wavenumber $k = \frac{2\pi\nu n}{c}$, q the particle charge, n the refractive index of the medium, R the distance and $\hat{r}$ the unit vector along the line of sight from observer to particle, and t_0' the retarded time of emission, while $\vec{\beta}^*$ is the non-zero velocity associated with the endpoint. '$\pm$' denotes a positive acceleration from rest to $\vec{\beta}^*$, or a negative acceleration from $\vec{\beta}^*$ to rest. In the time domain, the electric field seen by an observer $\vec{x}$ is given by:

$$\vec{E}_{\pm}(\vec{x},t) = \pm\frac{1}{\Delta t}\frac{q}{c}\left(\frac{\hat{r}\times\left[\hat{r}\times\vec{\beta}^*\right]}{(1-n\vec{\beta}^*\cdot\hat{r})R}\right), \tag{4.2}$$

with Δt the chosen scale of time resolution over which the electric field is averaged [11]. By dissecting the particle trajectories into enough track segments, and by stacking the endpoint emissions seen by an observer, the air shower's combined radio emission were simulated numerically. If an adequate step size is chosen for the simulation, the convertion of one doamin into the other with fast Fourier transformation (FFT) is possible, which allows the processing of the complete electron and positron distributons generated by CORSIKA, without any assumptions made on the emission mechanism itself [15]. The electric field is then calculated in the frequency domain for a total of 240 observers, that are positioned along the ground projection of a star-shaped grid aligned in the shower plane. Examples of this are shown in figure 16. The shower plane is spanned by the $\vec{v}\times\vec{B}$-axis and the $\vec{v}\times\vec{v}\times\vec{B}$-axis, with the direction of the incoming primary $\vec{v}$ being the shower axis, and $\vec{B}$ the magnetic field, and depending on the incoming direction, the ground projection can vary drastically in size, as can be seen in figure 16, reflecting the dimensions of the expected shower footprints seen in figure 9.
The CoREAS output was processed and saved to files, providing the possibility of simulating the hardware response of variable antenna and detecotor designs at a later time.
The set covers 6 primary energies $E \in \{10^{16}, 10^{16.5}, 10^{17}, 10^{17.5}, 10^{18}, 10^{18.5}\}$ eV and 17 arrival directions, with zenith $\theta \in \{5, 10, ..., 85\}$ deg and all at azimuth $\phi = 0$. Because Earth's magnetic field is close to perpendicular to the plane of the azimuth angle at summit station (declination 26.06°W, inclination 81.12° downwards), no variation of azimuth was included in

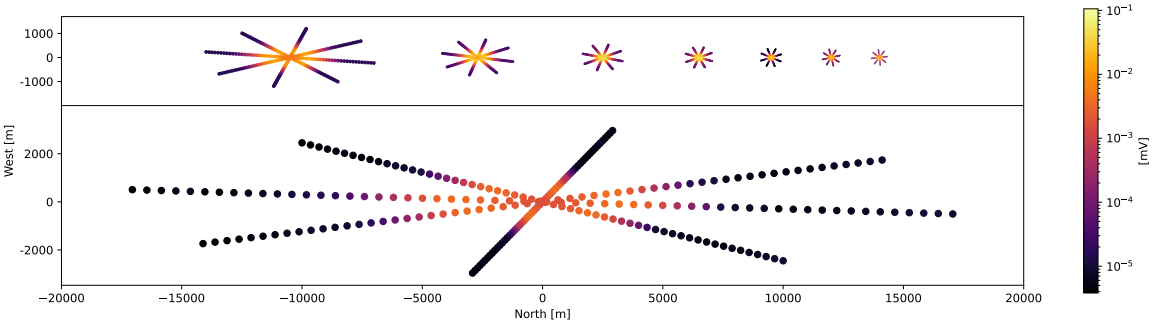

Figure 16: Maximum signal stength of channel 19 at every observer position in the star shaped grid, for CR events with energy $E = 10^{17}\,\mathrm{eV}$, arrival azimuth $\phi = 0$ and arrival zeniths $\theta \in [10, 80]$ deg, in 10 deg steps. Size of the shower footprint increases with zenith.

the simulations. Five air showers were simulated for each combination of energy E and zenith θ, which would have produced 510 files, and the files got assigned according indices of $[000, 509]$. For practical reasons, the files were sorted according to energy, zenith and a sample number $k \in [0, 4]$, and assigned a label accordingly (E, θ, k). As can be seen in figure 17a, only 407 of the simulations were successful, leaving gaps for some combinations of energy and zenith. Since the projected shape of the star shaped pattern and the observer positions only vary with zenith, and since the amplitude of the electric field at each observer is expected to scale linearly with shower energy, gaps in the grid can be closed. The shower footprint at an energy E_2 can be imitated, by using some of the files with the same zenith but from another energy level E_1 a second time, and then by scaling the signal strength accordingly by $\frac{E_2}{E_1}$. The files used multiple times for different grid spaces are shown in figure 17b.

4.2 Trigger simulations

NuRadioReco is a reconstruction framework for radio neutrino detectors such as RNO-G, and it offers a convenient way of accessing the stored CoREAS output and of running simulations on the hardware responses of antenna and detector models directly in python [8]. The hardware response functions, as well as the adding of radio background to the channel feed were also simulated using its modules.

The detector file of a single RNO-G station is loaded at each of the 240 observer positions of an air shower file, and afterwards the antenna impulse induced by the electric field is calculated in the frequency domain for each channel of the station, and is then obtained in the time

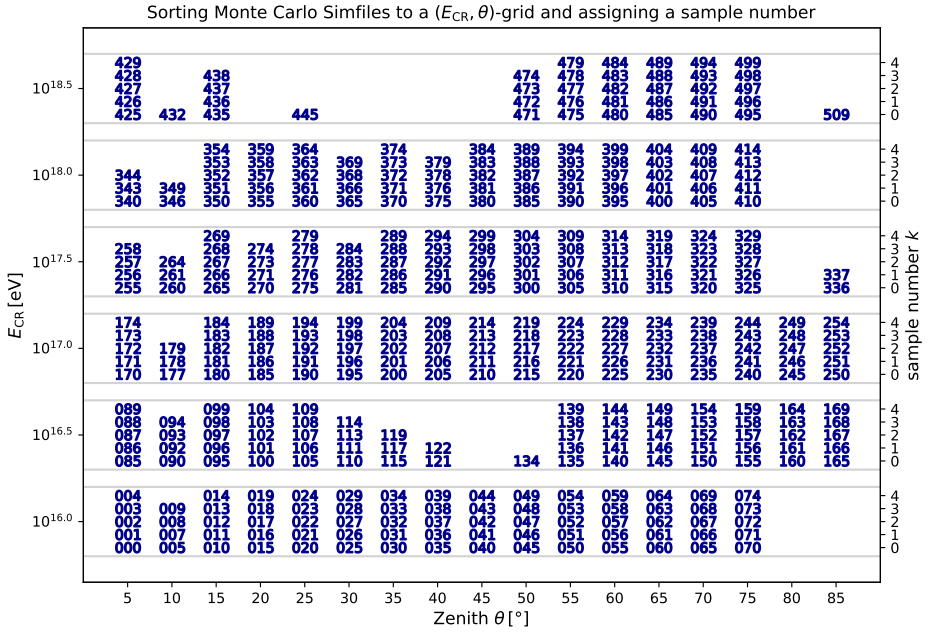

(a) Overview of Monte Carlo simulations available for each energy and zenith bin, listed by file index and sorted by new label (E, θ, k).

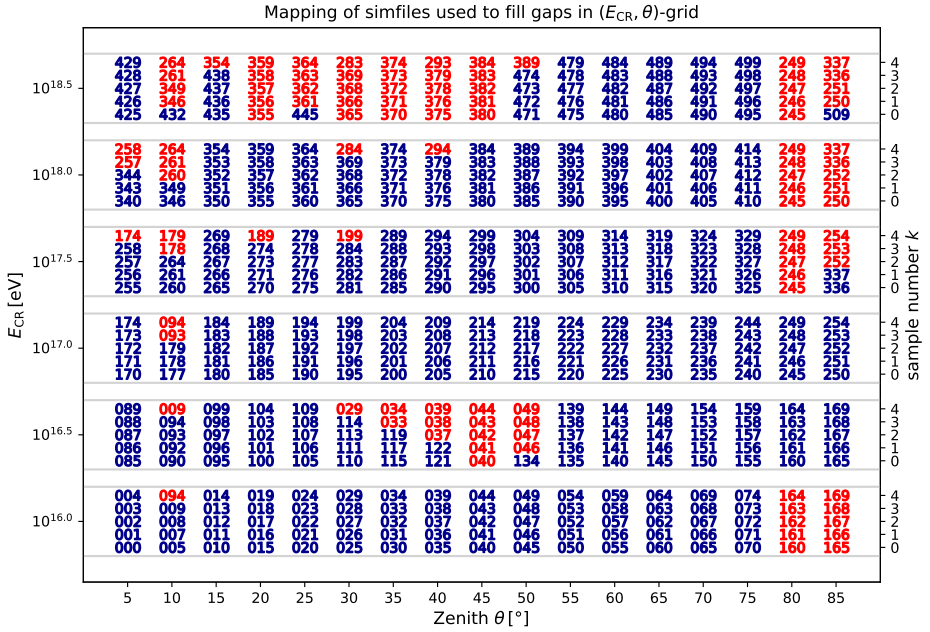

(b) Mapping of air shower simulation files used multiple times to close spaces in the energy zenith grid.

Figure 17

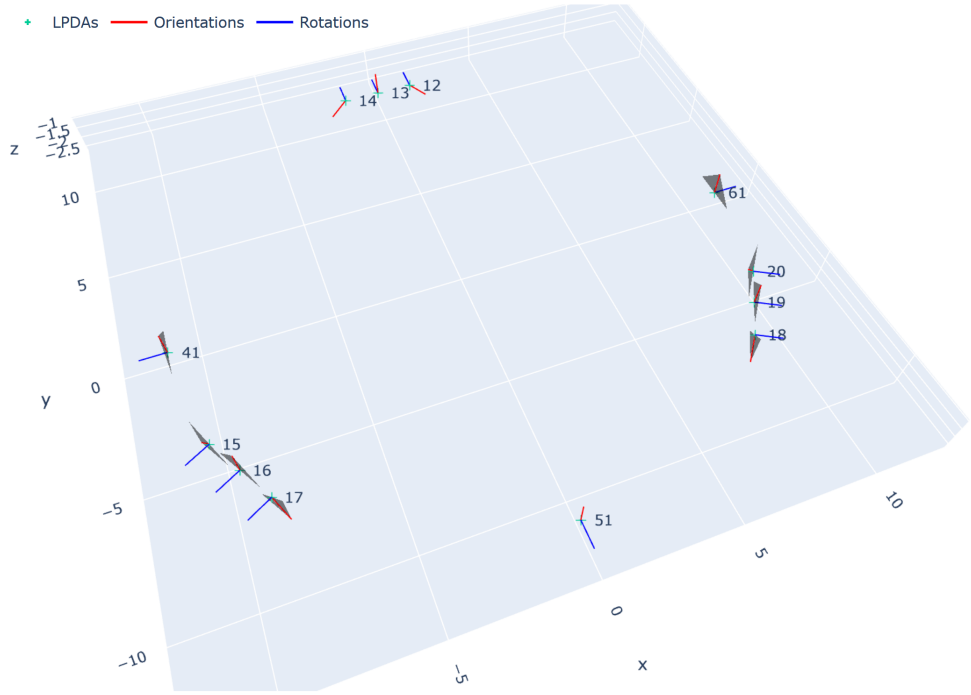

Figure 18: Single station layout, reduced only to surface channels, and added 3 updwards facing LPDAs to simulate square configuration simultaneously.

domain through FFT. If an air shower file is used again for another energy level than its own, the channel response will be rescaled accordingly. Following this, both radio noise from glactic sources and thermal noise is then added to the channel feed, using additional modules provided within the NuRadioReco library. Following the signal chain outlined in section 3.1, the signal impulse is then folded with the amplification function. At this point, the trigger simulation is run for trigger channels [13,16,19], with a two channel coincidence requirement, a 50 ns coincidence window, a $[0.08, 0.18]$ MHz passband trigger filter and a 30 mV trigger threshold. To save computational time, the layout of a RNO-G single station seen in figure 3 from section 3.1, was modified to only include the surface LPDA antennas. Furthermore, three additional upward facing LDPAs were added to the tested layout, which is shown in figure 18, so the trigger response of the triangular and square antenna configuration could be simulated simultaneously. Therefore, a second trigger simulation with identical settings is run for trigger channels [13,41,51,61].

The goal is to study the trigger efficiency of the triangular and square surface layout and to evaluate them in terms of total performance and directional consistency in azimuth, over a range of primary energies and arrival zeniths. In order to circumvent the immense computational resources needed to simulate complementary air shower sets for a similar range of energy and

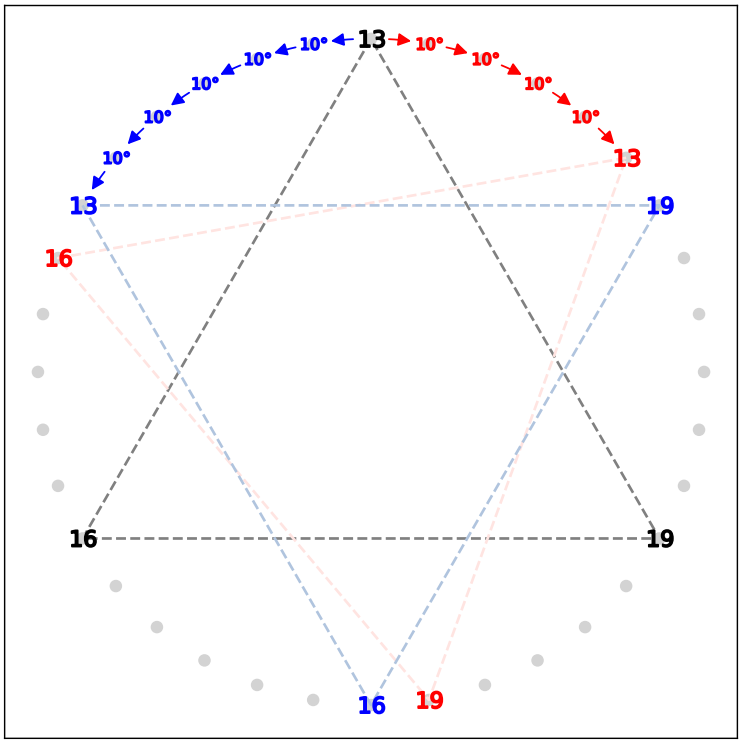

Figure 19: Layouts for eleven additional detector files. Antenna coordinates and alignments were rotated around the origin in 10 degree steps. Because the 3 antenna configuration is an equilateral triangle, after rotating by a total of 120°, it will be congruent to the original station design.

zenith at different arrival azimuths, the same set of air showers with $\phi = 0$ will be used repeatedly, while the antenna positions of the detector layout will be rotated in the azimuth plane. For this purpose, eleven additional detector files were created by rotating the layout in ten degree steps, covering a total of 120 degree and a third of the azimuth range. Because the triangular configuratrion is equilateral, the original layout is repeated after a 120 degree rotation, as can be seen in figure 19.

In total, 2937600 trigger simulations have been run, and each trigger decision was saved to a dataframe, so that they are accessible as a function of energy, zenith, azimuth, sample number, observer and antenna configuration:

$$\mathrm{TR} = \mathrm{TR}(E, \theta, \phi, k, \mathrm{Obs.}, \mathrm{Config.}) \ . \tag{4.3}$$

4.3 Differences between true arrival directions and rotation of detector layout

Rotating the detector layout works well for assessing its performance and finding potential blindspots when it comes to arrival directions, however, the difference, between this approximation and the actual conditions of a cosmic ray event from this arrival direction, itself is subject to the arrival direction. The deflection of the charged particles in the magnetic field is determined by the Lorentz force, and it has two direct effects on the impulse response of an antenna. There are two factors that are relatively easy to calculate, based on the differences in geometry, that have a direct influence on the strength and on the polarization of the geomagnetic emission.
With $\hat{v}$ and $\hat{B}$ as unit vectors along the shower axis and the magnetic field, respectively:

$$\hat{v} = \begin{pmatrix} -\sin\phi\sin\theta \\ -\cos\phi\sin\theta \\ -\cos\theta \end{pmatrix}, \ \hat{B} = \begin{pmatrix} \sin\phi_{\mathrm{B}}\sin\theta_{\mathrm{B}} \\ \cos\phi_{\mathrm{B}}\sin\theta_{\mathrm{B}} \\ \cos\theta_{\mathrm{B}} \end{pmatrix}, \ |\hat{v}\times\hat{B}| = \sin\alpha_1, \tag{4.4}$$

where $\theta_{\mathrm{B}} = -81.12$ deg -90 deg and $\phi_{\mathrm{B}} = 26.06$ deg are the alignment of the magnetic field, and α_1 is the angle between $\vec{v}$ and $\vec{B}$, which is given by:

$$\alpha_1 = \arccos\left(-\sin\theta\sin\theta_{\mathrm{B}}\cos\left(\phi-\phi_{\mathrm{B}}\right) - \cos\theta\cos\theta_{\mathrm{B}}\right). \tag{4.5}$$

Because the impulse response scales directly with the electric field of the emission, which in turn scales with the accelerating force on the particles [REF geomagnetic], that scales linearly with the sine function of the angle between $\vec{v}$ and $\vec{B}$ as, the following relation is true:

$$|\vec{E}| \propto |\vec{F}_B| \propto |\hat{v}\times\hat{B}| := \sin\alpha_1. \tag{4.6}$$

Therefore, the signal strength and the response of every channel scales with $\sin\alpha_1$, which would vary with the zenith and the azimuth of the arrival direction, as shown in figure 20. Because the detector rotates, instead of the arrival direction, this factor is kept constant at $\phi = 0$, and especially in the low to mid zenith range, this can make quite the difference. However, when loading the CoREAS output, the electric field cannot simply be factored by $\sin\alpha_1$ before folding it with the antenna response. Because the electron and positron distribution in the shower plane also changes with a stronger or weaker Lorentz force, the electric fields CoREAS would calculate would also change, resulting in different electric fields $\vec{E}$ seen by each observer in ways that

are hard to predict. So while the dispersion of field energy in the shower footprint will also become less or more centralized, the total field energy transferred into the electric field scales with $\sin\alpha_1(\phi)$, and therefore, the average signal response as well. Moreover, the contribution of the askaryan emission, as well as the varying influence of the cherenkov compression, as explained in section 2.3, is not taken into account.
The second difference in geometry that would influence the signal strength directly, is the direction of the polarization, as the emitted radiation is polarized along $\vec{v} \times \vec{B}$. The stongest response is induced in the antenna, when it is aligned with the oscillations of the electric field, therefore the response scales with the absolute value of the cosine of the angle α_2 between polarisation and the length of the antenna, which is given by:

$$\cos\alpha_2 = \hat{e}_a \cdot \frac{(\hat{v} \times \hat{B})}{|\hat{v} \times \hat{B}|} = \hat{e}_a \cdot \frac{(\hat{v} \times \hat{B})}{\sin\alpha_1}, \tag{4.7}$$

where $\hat{e}_a$ is a unit vector along the length of the antenna. Interestingly, this factor scales as an inverse of $\sin\alpha_1$.
Combining these two geometric factors, expecting that they both have linear proportionality with the channel impulse induced by the geomagnetic component, the following term is obtained:

$$\sin\alpha_1 |\cos\alpha_2| = |\hat{e}_a \cdot (\hat{v} \times \hat{B})|. \tag{4.8}$$

For fixed arrival directions and a rotated detector layout in the azimuth plane by $-\phi$, this term is:

$$\left| \begin{pmatrix} -\cos(\phi_a - \phi) \\ \sin(\phi_a - \phi) \\ 0 \end{pmatrix} \cdot \left(\begin{pmatrix} 0 \\ -\sin\theta \\ -\cos\theta \end{pmatrix} \times \begin{pmatrix} \sin\phi_\mathrm{B} \sin\theta_\mathrm{B} \\ \cos\phi_\mathrm{B} \sin\theta_\mathrm{B} \\ \cos\theta_\mathrm{B} \end{pmatrix} \right) \right|, \tag{4.9}$$

with ϕ_a the rotation of the antenna in the azimuth plane. And for true arrival directions with a stationary detector layout, the term is:

$$\left| \begin{pmatrix} -\cos\phi_a \\ \sin\phi_a \\ 0 \end{pmatrix} \cdot \left(\begin{pmatrix} -\sin\phi\sin\theta \\ -\cos\phi\sin\theta \\ -\cos\theta \end{pmatrix} \times \begin{pmatrix} \sin\phi_\mathrm{B} \sin\theta_\mathrm{B} \\ \cos\phi_\mathrm{B} \sin\theta_\mathrm{B} \\ \cos\theta_\mathrm{B} \end{pmatrix} \right) \right|. \tag{4.10}$$

Averaging these terms over ϕ, an estimate for how each channel response simulated with true arrival directions would scale to the simulated response of rotated detector layouts, is obtained by $\frac{\mu_\phi(\text{term 4.10})}{\mu_\phi(\text{term 4.9})}$ as a function of zenith, which is shown in figure 21.
Again it has to be emphasized, that this factor cannot be folded with the signal response during

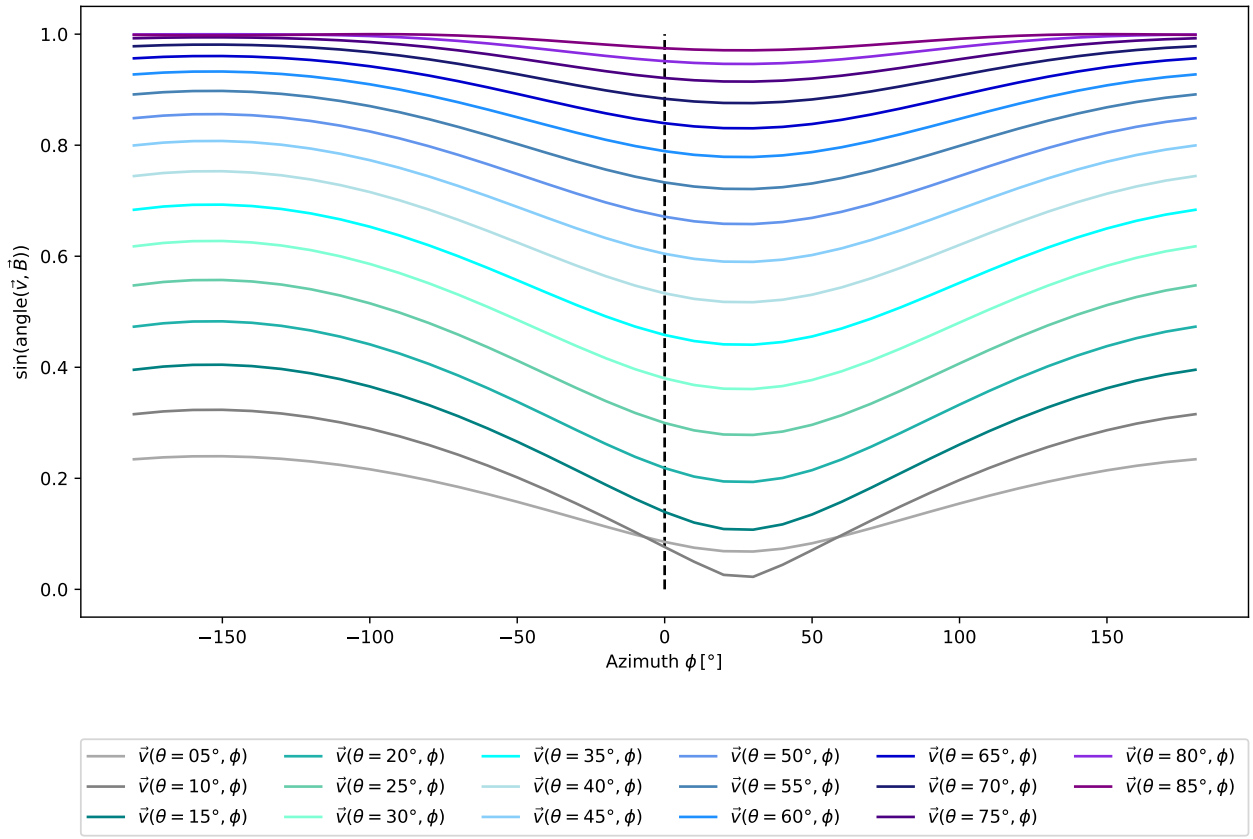

Figure 20: Sine of angle($\vec{v}, \vec{B}$) $\sin \alpha_1$, as a series of functions of azimuth ϕ.

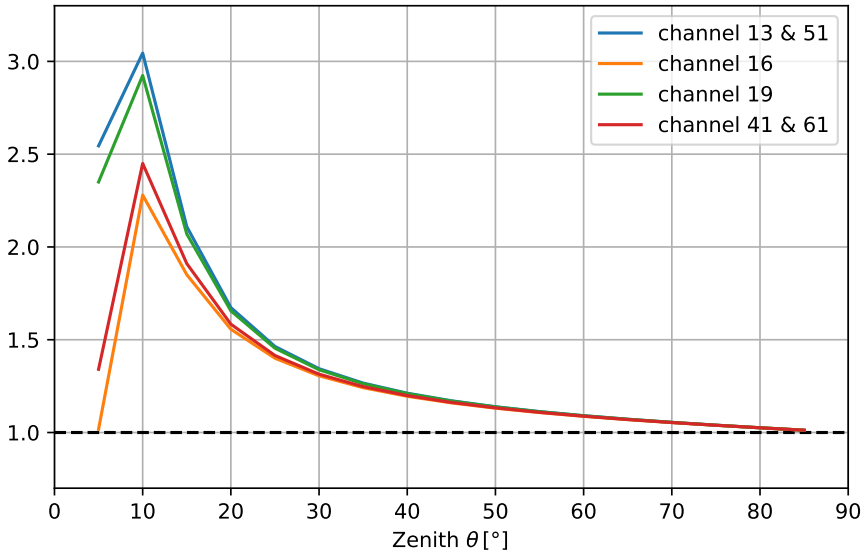

Figure 21: Graphic considerations on the relative strength of the geomagentic emission. Factor $\frac{\mu_\phi(\text{term } 4.10)}{\mu_\phi(\text{term } 4.9)}$, scale of channel impulse (induced by geomagnetic component) simulated with true arrival directions to channel impulses simulated with rotated detecors, averaged over the azimuth spectrum. Estimation based on geometric differences.

the simulation, before the trigger simulation is conducted for the station, to obtain accurate results for the trigger rate. It is an average for all observers, and an average over the entire azimuth spectrum, and it does not take the probably noticable changes to the energy dispersion within the shower footprint into account. Especially at the link between field strength, signal strength and trigger decision, while fairly straightforward for a single observer, it becomes hard to estimate how a more strongly or weakly concentrated distribution of shower energy around its axis will result in changes to the rate of triggered observers over the entire area of the footprint. Apart from this, it only applies to the strength of the geomagnetic emission, which is, while dominant, not the only source of radio emission. It is therefore no substitution for accurate quanitative results obtained through simulating for a much more extensive set of air showers covering all true arrival directions.

However, from graphic consideration of figure 20, it becomes clear that the energy dispersion in the shower footprint changes much less with azimuth for the mid to high zenith range, as the strength of the Lorenz force scales with $\sin\alpha_1$. Furthermore, the combined and averaged deviation of the signal strength, from geomagnetic emission, expected from an accurate $|\vec{v}\times\vec{B}|$ component and an accurate polarization and channel alignment, is also much smaller for the mid to high zenith range, as it was shown in figure 21. Therefore, the results obtained from the

approach used in this thesis will nontheless give a good estimate on the expected trigger rate at mid to high zeniths.

5 Trigger efficiency results

Because of the multitude of parameters (energy, zenith, azimuth, observer position), that each have their respective influence on the trigger decision, there are multiple ways to formulate a trigger efficiency in respect to the spectrum of a specific parameter. Of special interest are the consistency and the sum of the trigger performance over the azimuth range, of the 3 and 4 antenna trigger configurations respectively. A detailed comparative analysis of the total performance, as well as of the performance at specific energy and zenith combinations will follow in the sections 5.2 to 5.5.

5.1 Weighting and summation of discreet bins

To formulate a quantitative trigger efficieny for a certain paramater range, the simulated paramter combinations must be treated as discreet bins and attributed a respective weight. For example are CR events with primary energy $10^{18}\,\mathrm{eV}$ about 10000 times less likely than CR events at $10^{16}\,\mathrm{eV}$, although they might be much more likely to successfully trigger as they have a 100 times more energy. Similarly are arrival directions from greater zeniths more likely, as they span a greater solid angle, as can be seen in figure 23.
With $J(E)$ the energy differential of the flux of cosmic rays, the flux of CR events within a discreet energy bin is given by:

$$\begin{aligned} w_\mathrm{E} &= \int_{E\cdot 10^{-0.25}}^{E\cdot 10^{+0.25}} J(E')\,\mathrm{d}E', \\ [J(E)] &= \mathrm{eV}^{-1}\,\mathrm{m}^{-2}\,\mathrm{ns}^{-1}\,\mathrm{sr}^{-1}, \\ [w_\mathrm{E}] &= \mathrm{m}^{-2}\,\mathrm{ns}^{-1}\,\mathrm{sr}^{-1}. \end{aligned} \tag{5.1}$$

Choosing a logarithmic width of the energy bins matches the simulation set used, as it provided a resolution of energy at logarithmic $10^{+0.5}$ steps. The resulting bin weights are presented in figure 22. The curve for $J(E)$ was taken from the 2019 measurement results of the cosmic ray

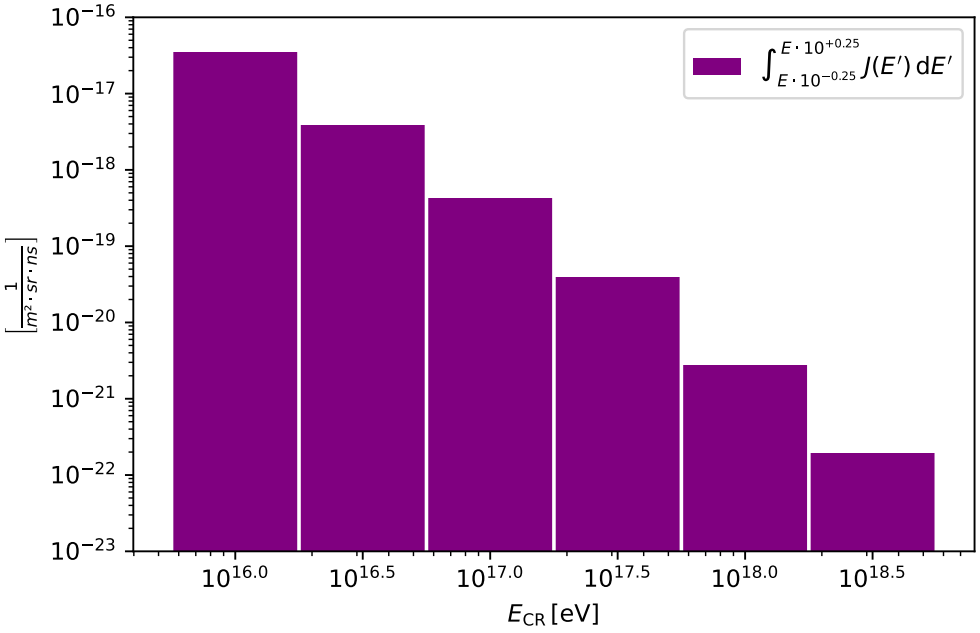

Figure 22: Cosmic ray flux w_{E} per energy bin.

flux, conducted by the Pierre Auger Observatory in 2019 [6].
The possible arrival direction of a CR-Event from the reference point of the observer is expressed in coordinates of zenith θ and azimuth ϕ, and their entire range spans a solid angle of:

$$\Omega = \int_{[0,\frac{\pi}{2}]} \int_{[-\pi,\pi]} \sin\theta \, \mathrm{d}\theta \, \mathrm{d}\phi = 2\pi \, \mathrm{sr}. \tag{5.2}$$

The simulations are run for zeniths $[5, 85]$ deg in 5 degree steps, which equals 17 discreet zenith bins with a binwidth of 5 degree, and for 12 detector rotations, which are, due to the periodicy of rotating the triangular surface layout, the equivalent of 36 discreet azimuth bins with a width of 10 degrees.
Because of the even distribution of the azimuth, the weight of an azimuth bin is constant:

$$w_\phi = \int_{\phi-5\,\mathrm{deg}}^{\phi+5\,\mathrm{deg}} \mathrm{d}\phi' = \frac{2\pi}{36}\mathrm{rad}, \tag{5.3}$$

while the weight of a zenith bin is not:

$$\begin{aligned} w_\theta &= \int_{\theta-2.5\,\mathrm{deg}}^{\theta+2.5\,\mathrm{deg}} \sin\theta' \, \mathrm{d}\theta', \\ [w_\theta] &= \mathrm{rad}. \end{aligned} \tag{5.4}$$

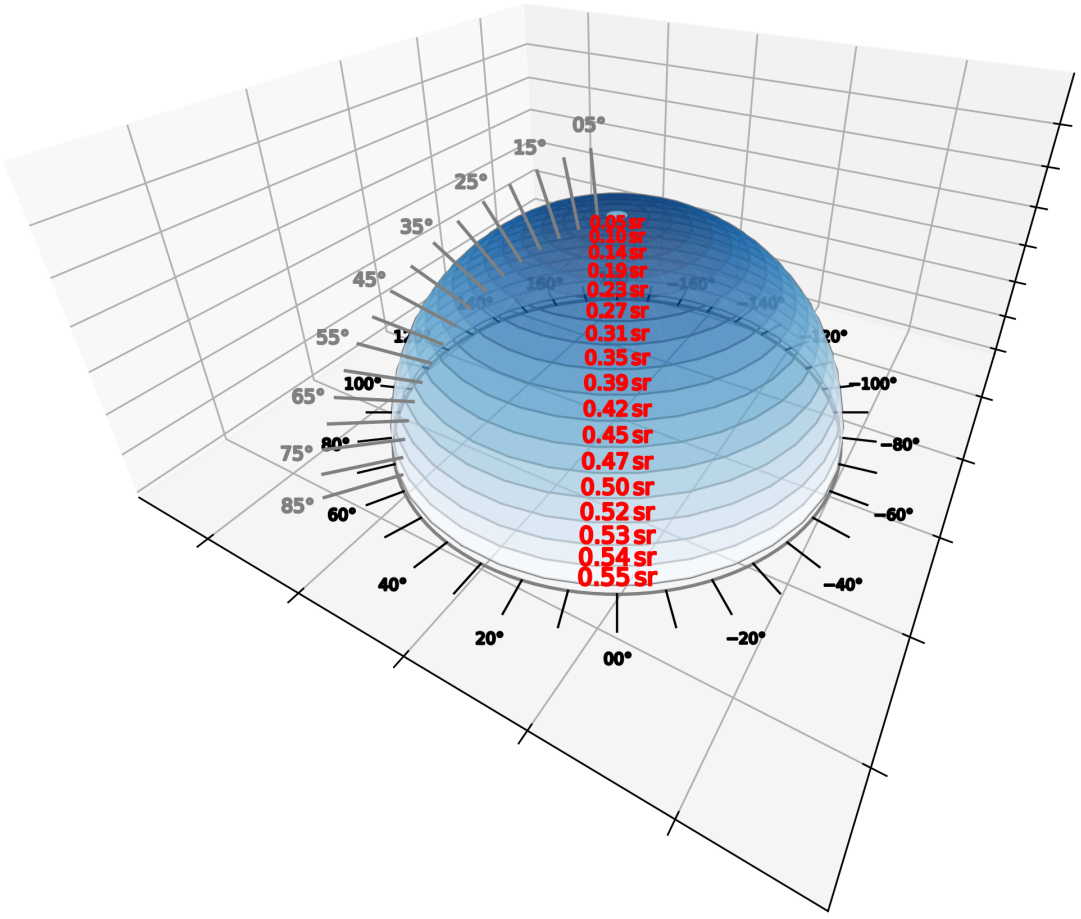

Figure 23: Visualization of distribution of solid angle per zenith bin. Higher zeniths span a greater solid angle.

A visualization of this is presented in figure 23, while the values of w_θ are depicted in figure 24.

The weight of a single observer position matches the area resolution resulting from dissecting the projection of the shower footprint into 240 pieces. The area bin associated with an observer is every point on the ground that is closer to them than to any other observer. The resulting area cells A_{obs} were already calculated and accessible in the simulation files that have been provided for this study. As can be seen in figure 25, the projected area cells increase significantly in scale with higher zenith. Since the flux of cosmic rays passes not vertically through this area, but at the angle of the arrival zenith, the actual area weight of an observer is the effective area through which cosmic rays at this arrival zenith pass. The area weight of an observer is

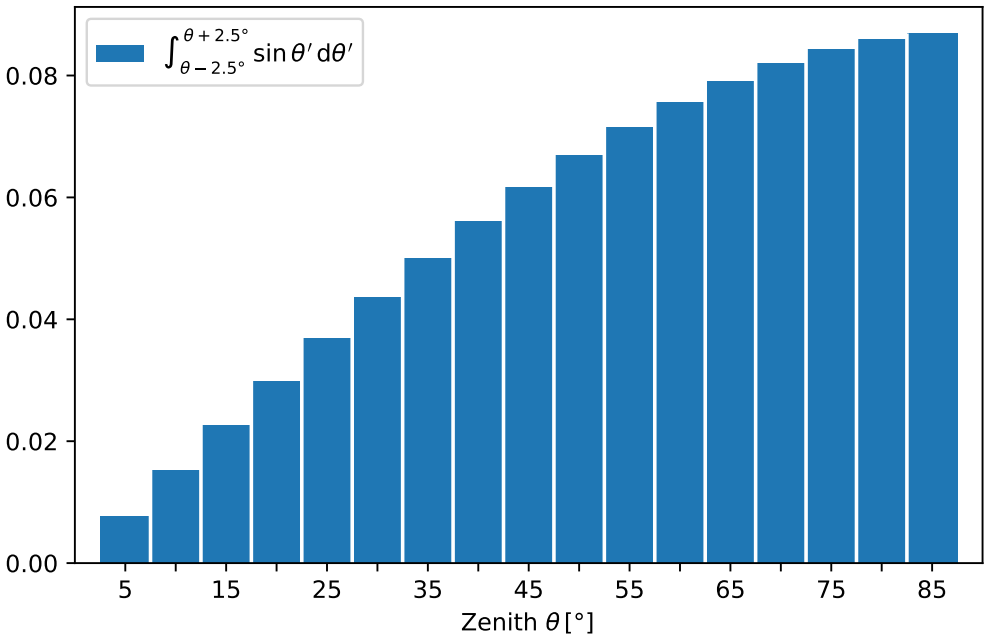

Figure 24: Weight w_θ of discreet zenith bins.

therefore the area of the ground projection factored with the cosine of the arrival zenith:

$$\begin{aligned} A^{\text{eff}}_{\text{Obs.}} &= \cos(\theta) A_{\text{Obs.}}, \\ [A^{\text{eff}}_{\text{Obs.}}] &= \text{m}^2. \end{aligned} \tag{5.5}$$

While the cosine factor becomes 0 at $\theta = 90$ deg, the effective area of the shower footprint still climbs steeply up to the highest simulated arrival zenith at $\theta = 85$ deg, as can be seen in figure 26.

Combining the obtained flux of CR events in an energy bin, with the bin weights associated with an arrival direction and an observer cell, the expected rate of CR events is then given by:

$$\dot{N}_{\text{CR}}(E, \theta, \phi, \text{Obs.}) = \int_{E \cdot 10^{-0.25}}^{E \cdot 10^{+0.25}} J(E') \, \text{d}E' \cdot \frac{2\pi}{36} \int_{\theta - 2.5\,\text{deg}}^{\theta + 2.5\,\text{deg}} \sin\theta' \, \text{d}\theta' \cdot \cos(\theta) A_{\text{Obs.}}. \tag{5.6}$$

For a visualization of the distribution of bin weights, the rate of being within the area of a shower footprint with specific incident energy and zenith, which is given by:

$$\dot{N}_{\text{CR}}(E, \theta) = \int_{E \cdot 10^{-0.25}}^{E \cdot 10^{+0.25}} J(E') \, \text{d}E' \cdot 2\pi \int_{\theta - 2.5\,\text{deg}}^{\theta + 2.5\,\text{deg}} \sin\theta' \, \text{d}\theta' \cdot \cos(\theta) \sum_{\text{Obs.}=0}^{239} A_{\text{Obs.}}. \tag{5.7}$$

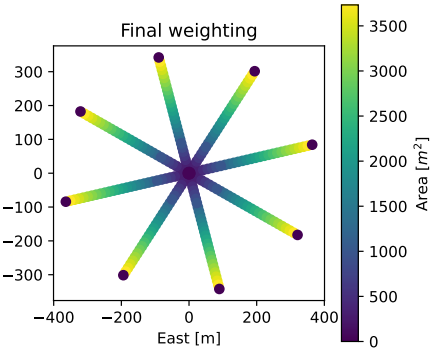

(a) Star grid projection at arrival zenith $\theta = 20$ deg

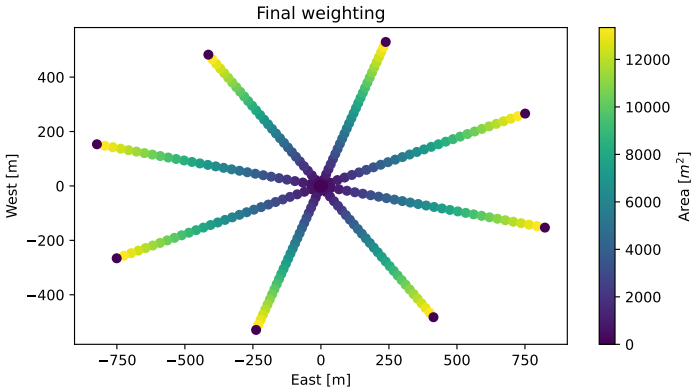

(b) Star grid projection at arrival zenith $\theta = 50$ deg

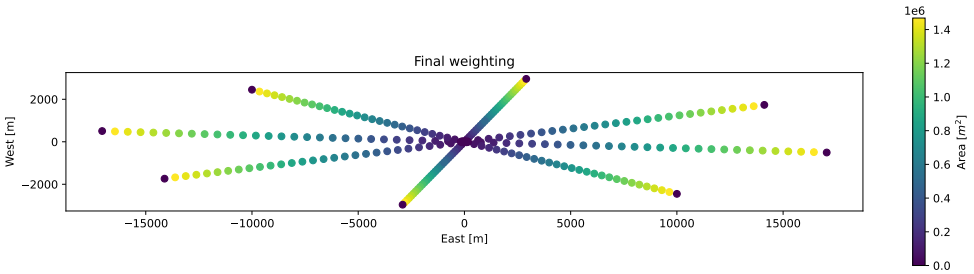

(c) Star grid projection at arrival zenith $\theta = 80$ deg

Figure 25: Area cells attributed to each observer A_{obs} for a selection of various arrival zeniths. Please note the difference in scale of the colorbars.

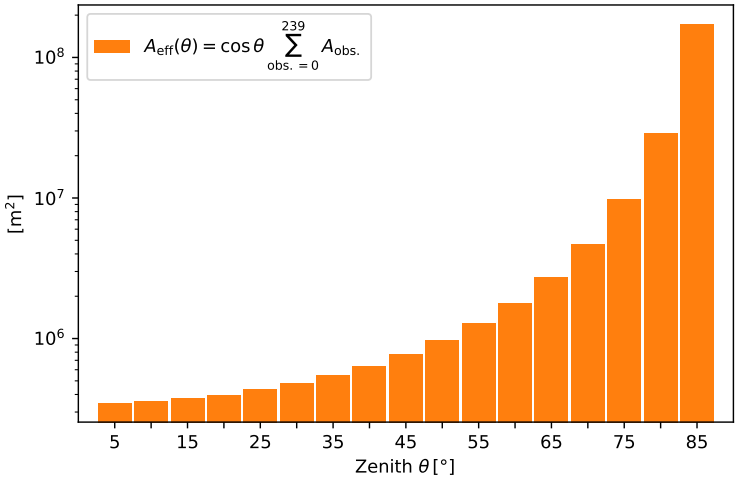

Figure 26: Effective projected area of the simulated air shower footprints as a function of zenith.

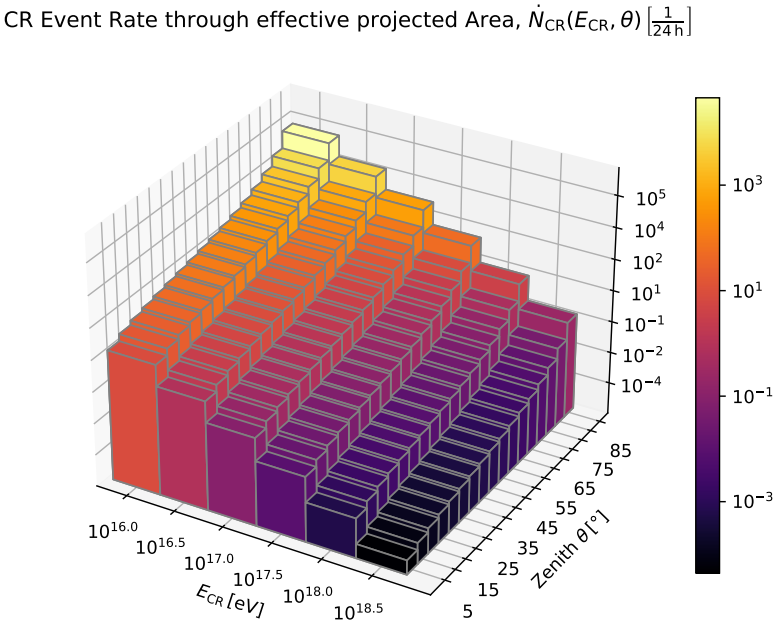

Figure 27: Visualization of bin weight distribution. Rate of CR events observed from each energy and zenith bin $\dot{N}_{\mathrm{CR}}(E, \theta)$, in units of $\left[\frac{1}{24\,\mathrm{h}}\right]$.

For visualization it has been depicted in figure 27.
The trigger decision extracted from the dataframe "$\mathrm{TR}(E_{\mathrm{CR}}, \theta, \phi, k, A_{\mathrm{Obs.}})$" is then simply weighted with 1 if true or 0 if false. Finally, the single station trigger rate $X(E, \theta, \phi, \mathrm{Obs.})$ at which the simulated detector station would then be triggered, by a CR event from the energy bin E_{CR}, zenith bin θ and azimuth bin ϕ, and with a trajectory relative to the postion of the station such that it is inside the area cell $A_{\mathrm{Obs.}}$ of the projected shower footprint, is then given by:

$$\begin{aligned} X(E_{\mathrm{CR}}, \theta, \phi, A_{\mathrm{Obs.}}) = \\ w_{\mathrm{E}} \cdot w_{\theta} \cdot w_{\phi} \cdot \cos(\theta) A_{\mathrm{Obs.}} \cdot \sum_{k=0}^{4} \frac{1}{5} \cdot \mathrm{TR}(E_{\mathrm{CR}}, \theta, \phi, k, A_{\mathrm{Obs.}}), \end{aligned} \tag{5.8}$$

averaged over the 5 simulation file samples for each (E, θ)-bin combination, as they were assigned in figure 17b.
In the following sections, if the trigger rate X is given as a function of its variables, it is referring to the trigger rate for cosmic ray events within one bin each of the specfied variables. If it is not written as a fuction of one of its variables, it is referring to the trigger rate for cosmic ray events within the entire simulated range of that variable, which is simply the sum of its bins:

$$X(a, b) = \sum_{c=c_{\mathrm{min}}}^{c_{\mathrm{max}}} X(a, b, c). \tag{5.9}$$

The calculation of the mean value and the standard variation of the trigger rate in regards to the spectrum of one variable are denoted as:

$$\begin{aligned} \mu_{\mathrm{c}}(a, b) =& \frac{1}{N_{\mathrm{c}}} \sum_{c} X(a, b, c) \\ \sigma_{\mathrm{c}}(a, b) =& \sqrt{\frac{1}{N_{\mathrm{c}}} \sum_{c} (X(a, b, c) - \mu_{c}(a, b))^2}. \end{aligned} \tag{5.10}$$

5.2 Analysis of trigger rate as a function of azimuth

For a comparative analysis of the trigger efficiency as a function of azimuth, we need to obtain the trigger rate of the single station in each azimuth bin $X(\phi)$, by summing the trigger rates

of the entirety of the energy and the zenith range, and for all simulated observers:

$$X(\phi) = \\ w_\phi \cdot \sum_{E=10^{16}\,\mathrm{eV}}^{10^{18.5}\,\mathrm{eV}} w_\mathrm{E} \cdot \sum_{\theta=5\,\mathrm{deg}}^{85\,\mathrm{deg}} w_\theta \cdot \cos(\theta) \sum_{\mathrm{Obs.}=0}^{239} A_\mathrm{Obs.} \cdot \sum_{k=0}^{4} \frac{1}{5} \cdot \mathrm{TR}(E_\mathrm{CR}, \theta, \phi, k, A_\mathrm{Obs.}). \tag{5.11}$$

The according values for $X_{(3\mathrm{conf})}(\phi)$ and $X_{(3\mathrm{conf})}(\phi)$ are both depicted in figure 28, which shows that the 4 array has an overall higher and more consistent trigger efficiency. In qualtity, the trigger rates behave very similar to the function of the second largest cross section between E-field polarization and the trigger channel antenna of each configuration, as it was shown in figure **??**, which suggests a proportionality between the second strongest signal strength and the trigger efficiency, at least over the broad range of all possible energy and zenith combinations. As a comparable and quantitative measure of trigger sensitivity, the total trigger rate for CR events of the entire simulated range of its variables is calculated as

$$X = 3 \cdot \sum_{\phi=-50\,\mathrm{deg}}^{60\,\mathrm{deg}} X(\phi), \tag{5.12}$$

by summing over the 12 simulated azimuth bins and multiplying by 3, as only a third of the azimuth range was simulated, to cover the entire 360 deg range. As a comparable measure of directional sensitivity with azimuth, the relative standard deviation of the trigger rate is calulated as

$$\sigma_\phi^\mathrm{rel.} = \frac{\sigma_\phi}{\mu_\phi}, \tag{5.13}$$

with mean and standard deviation from equation 5.10. The 3 antenna configuration has a total trigger rate of $X_{(3\mathrm{conf})} = 2.7\,\frac{1}{(24\,\mathrm{h})}$ and a relative deviation with azimuth of $\sigma^\mathrm{rel.}_{\phi,\,(3\mathrm{conf})} = 0.3$, while the 4 antenna configuration has a total rate of $X_{(4\mathrm{conf})} = 3.69\,\frac{1}{(24\,\mathrm{h})}$ and a deviation $\sigma^\mathrm{rel.}_{\phi,\,(4\mathrm{conf})} = 0.12$.
In comparison, the 4 antenna layout has 37.0 % larger detection rate and a 53.0 % smaller deviation.
When deployed with the same trigger threshold, the 3 antenna layout performs considerably worse in terms of total trigger rate and uniformity of trigger rate in azimuth.

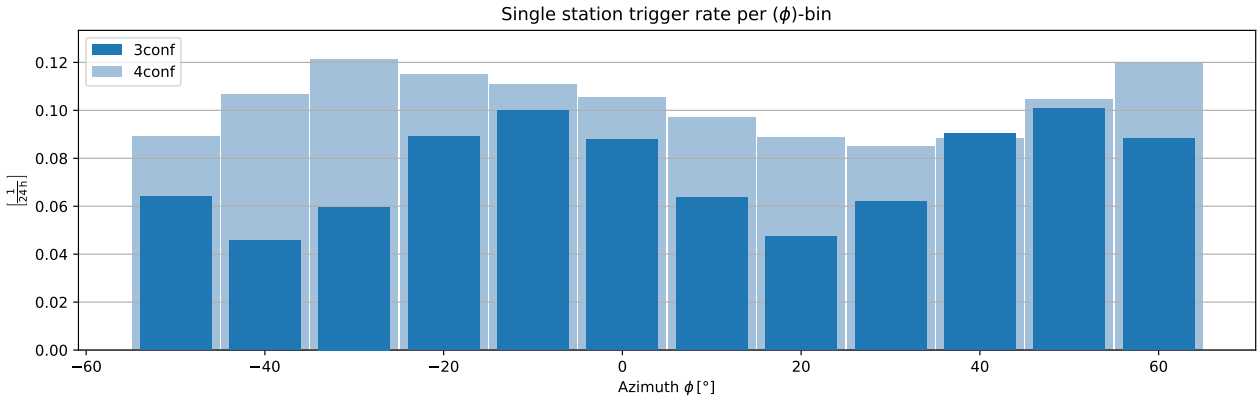

Figure 28: Single station trigger rate in each of the simulated azimuth bins, in units of $\left[\frac{1}{24\,\mathrm{h}}\right]$, calculated according to equation 5.11. The translucent bars show $X_{(4\mathrm{conf})}(\phi)$, while the solid bars show the values of $X_{(3\mathrm{conf})}(\phi)$. The trigger rate of the 4 antenna configuration is overall higher, and it is more uniform in azimuth.

5.3 Analysis of trigger rate as a function of energy and azimuth

To take a closer look at how the trigger rate is influenced by azimuth specifically at each energy level, the trigger rate within an energy and an azimuth bin is calculated as:

$$X(E,\phi) = w_\phi \cdot w_\mathrm{E} \cdot \sum_{\theta=5\,\mathrm{deg}}^{85\,\mathrm{deg}} w_\theta \cdot \cos(\theta) \sum_{\mathrm{Obs.}=0}^{239} A_{\mathrm{Obs.}} \cdot \sum_{k=0}^{4} \frac{1}{5} \cdot \mathrm{TR}(E_\mathrm{CR}, \theta, \phi, k, A_{\mathrm{Obs.}}). \tag{5.14}$$

The results for both configurations are shown in figure 29a. To obtain a comparable, quantitative measure of trigger efficiency at each energy level, $X(E)$ is calculated by summation of $X(E,\phi)$ over the azimuth range, as it was done for $X(\phi)$ with equation 5.12 in the previous section. The results can be seen in figure 29b. Both are unable to make any detections at the lowest energy level, and both have their highest detection rate at energy level $E = 10^{17.5}\,\mathrm{eV}$. The relative difference between the two becomes gradually smaller with energy, as the 3 antenna layout comes closer to the efficiency level of the 4 antenna layout at higher energy levels. This is because the projected area of an observer cell increases with the square of the distance from the shower axis, and those observers that are the farthest from the shower axis and are still triggered make up significant parts of the sum, as can be seen from figure 25. However, since the field strength of the projected air shower front decreases with distance from the shower axis

as well, those are also the trigger decisions that barely met the threshold criteria. Rotating either the channel antennas or the polarization in the azimuth plane may decrease or increase their respective signal strenght by the same relative factor at every observer position. But due to the required two channel coincidence, this will only result in a change of trigger decision if the second strongest channel response is close to the trigger threshold criteria. Therefore the trigger decision will almost exclusively change for these outer observers with a changing azimuth. As the energy level increases, so does the energy density of the entire shower footprint, and more rings of observers will trigger. The outermost ring of observers that will still trigger will not make up as big of a portion of the triggered area as for lower energies, because there are more rings of observers towards the center that will trigger consistently, and are less vulnerable to changes in azimuth.
This is also the reason the relative deviation in azimuth as a function of energy, decreases with energy for both layouts, as can be seen in figure 29c. The relative deviation in azimuth at each energy level is calculated, with mean and standard deviation according to equation 5.10, as:

$$\sigma_{\phi}^{\text{rel.}}(E) = \frac{\sigma_{\phi}(E)}{\mu_{\phi}(E)}. \tag{5.15}$$

The directional trigger sensitivity of both configurations becomes much more uniform in azimuth for a greater shower energy. However, the deviation with azimuth of the 4 antenna configuration $\sigma^{\text{rel.}}_{\phi,\,(4\text{conf})}(E)$ always remains 25% to 50% smaller than that of the 3 antenna configuration $\sigma^{\text{rel.}}_{\phi,\,(3\text{conf})}(E)$, on every energy level with detection. No pattern for the relative difference $\frac{\sigma^{\text{rel.}}_{\phi,\,(4\text{conf})}(E)}{\sigma^{\text{rel.}}_{\phi,\,(3\text{conf})}(E)} - 1$ becomes apparent, suggesting an independence from shower energy, or at least a neglectable relation for the simulated range. Therefore it can be concluded, that the trigger rate as function of azimuth is always less uniform for the 3 antenna array, independent of shower energy, and independent of better trigger performance at higher energy levels.

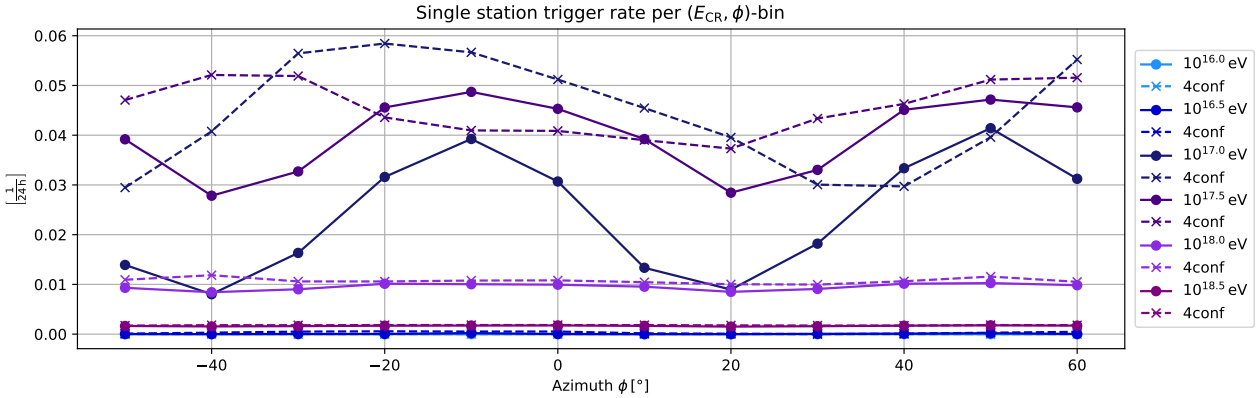

(a) Single station trigger rate in every energy and azimuth bin, from equation 5.14, as a series in E of funcions of ϕ, in units of $\left[\frac{1}{24\,\mathrm{h}}\right]$. $X_{(3\mathrm{conf})}(E,\phi)$ are plotted as dots and connected by full lines, while $X_{(4\mathrm{conf})}(E,\phi)$ are plotted as crosses and connected by dashed lines.

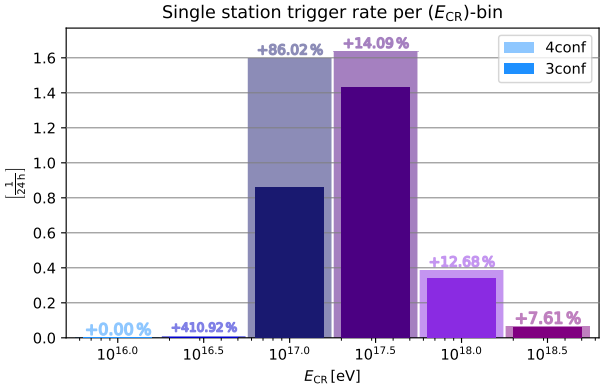

(b) Single station trigger rate in every energy bin, by summation $\sum_\phi X(E,\phi)$ of all azimuth bins, according to equation 5.9, in units of $\left[\frac{1}{24\,\mathrm{h}}\right]$. The solid bars show the results for $X_{(3\mathrm{conf})}(E)$, while the translucent bars show $X_{(4\mathrm{conf})}(E)$. The relative difference $\frac{X_{(4\mathrm{conf})}(E)}{X_{(3\mathrm{conf})}(E)} - 1$ is written above the respective bars. With increasing shower energy, the trigger rate of 3 antenna configuration comes closer to the efficiency level of 4 antenna configuration.

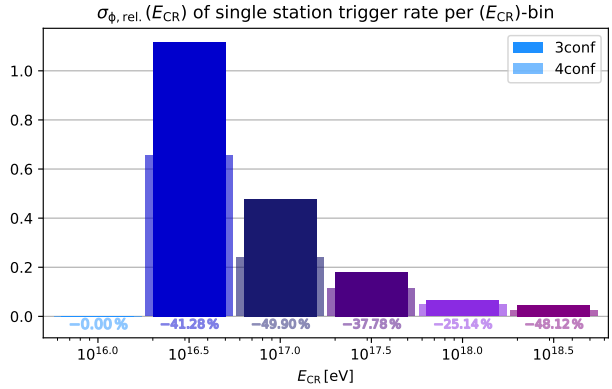

(c) Relative deviation of $X(E,\phi)$ with azimuth in every energy bin, as calculated in equation 5.15. The solid bars show the results for $\sigma^{\mathrm{rel.}}_{\phi,\,(3\mathrm{conf})}(E)$, while the translucent bars show $\sigma^{\mathrm{rel.}}_{\phi,\,(4\mathrm{conf})}(E)$. The relative difference $\frac{\sigma^{\mathrm{rel.}}_{\phi,\,(4\mathrm{conf})}(E)}{\sigma^{\mathrm{rel.}}_{\phi,\,(3\mathrm{conf})}(E)} - 1$ is written below the respective bars. While uniformity of trigger rate in azimuth improves greatly for both with rising shower energy, the 4 antenna configuration has an at least 25% smaller deviation at every energy level.

Figure 29: Analysis at every energy level of single station trigger rate $X(E,\phi)$ as a function of azimuth.

5.4 Analysis of trigger rate as a function of zenith and azimuth

Like in the previous sections, by summation of the ramaining variables, the trigger rate in each zenith and azimuth bin is obtained as

$$X(\theta,\phi) = \\ w_\phi \cdot w_\theta \cdot \sum_{E=10^{16}\,\mathrm{eV}}^{10^{18.5}\,\mathrm{eV}} w_\mathrm{E} \cdot \cos(\theta) \sum_{\mathrm{Obs.}=0}^{239} A_{\mathrm{Obs.}} \cdot \sum_{k=0}^{4} \frac{1}{5} \cdot \mathrm{TR}(E_\mathrm{CR}, \theta, \phi, k, A_{\mathrm{Obs.}}), \tag{5.16}$$

which are shown in figure 30a and 30b, for 3 and 4 antenna design respectively. A three dimensional visualization can be found in figure 31. Summation of the azimuth range is shown in figure 30c and the relative standard deviation

$$\sigma_\phi^{\mathrm{rel.}}(\theta) = \frac{\sigma_\phi(\theta)}{\mu_\phi(\theta)}, \tag{5.17}$$

is depicted in figure 30d.

The 4 antenna configuration performs 46-80% better in the low to mid zenith range $\theta \in [5, 50]\,\mathrm{deg}$, and 9-18% better at higher zeniths $\theta \in [60, 75]\,\mathrm{deg}$. This is because the higher zenith range is the main contributer for greater shower energies, where the 3 antenna configuration performs closer to the level of the 4 antenna configuration, which was previously explained in section 5.3. This can be seen in figure 32 and 33, where the trigger rates are shown as a function of energy and zenith. Trigger rates climb from the low and the high zenith range towards the peaks at $\theta = 45\,\mathrm{deg}$ and at $\theta = 65\,\mathrm{deg}$.

As it was explained in section 4.3, it has to be kept in mind that the geomagnetic emission would deviate noticably in strength and polarization in the lower zenith range. Therefore, the trigger rate as a function of zenith θ and azimuth ϕ, as it is depicted in figure 30a, 30b, 31 and 33, could look different in shape and amplitude for the lower zenith range, if Monte Carlo simulations with true arrival directions, that included variation over the entire azimuth range, had been used. As the low zenith range up to ~ 30 deg only accounts for 8.3 % and 9.1 % of the total trigger rate, respectively for 3 and 4 configuration, it has a neglectable contribution to the results delivered in section 5.2. While the inaccuracy of $X(\theta)$ and $\sigma_\phi^{\mathrm{rel.}}(\theta)$ in the lower zenith range is more unpredictable, given their small detection rate, no significant changes are to be expected to the total trigger rate X, and neither to $X(E)$ at the higher energy levels, where the mid to high zenith range is dominant, as can be seen in figure 32. For a truly

accurate prediction of trigger rates in each of the simulated bins, an accordingly more extensive set of Monte Carlo simulations would be needed for each azimuth bin. An estimation of correction by means of proper error propagation is not possible due to the complexity of the Monte Carlo simulations. For the scope of this study however, the performance levels of the 3 antenna and the 4 antenna layout were analysed for a broad variety of energy and trajectory of air shower events, and the determined trigger rates provide sufficent results to judge their respective efficiency and uniformity.

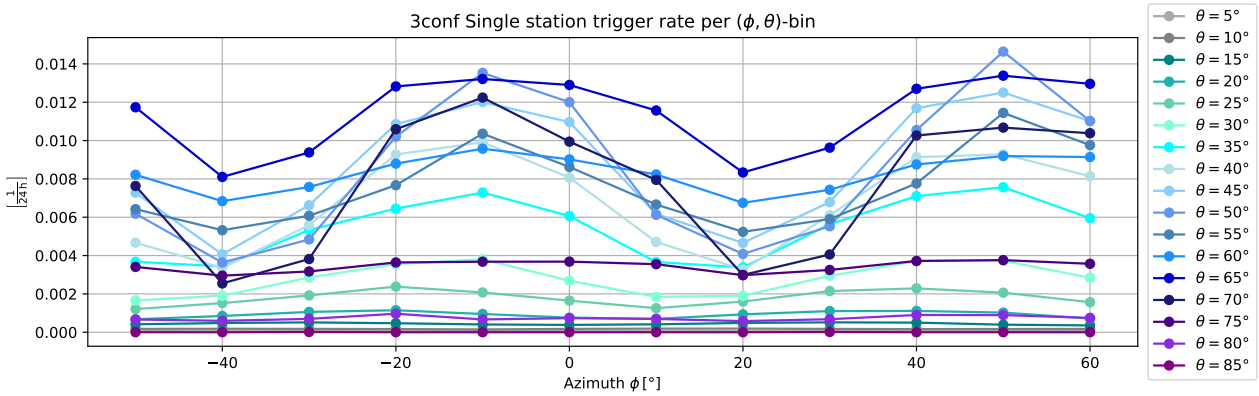

(a) Single station trigger rate for 3 antenna configuration, in every zenith and azimuth bin, $X_{(3\text{conf})}(\theta, \phi)$ from equation 5.16, as a series in θ of funcions of ϕ, in units of $\left[\frac{1}{24\,\text{h}}\right]$.

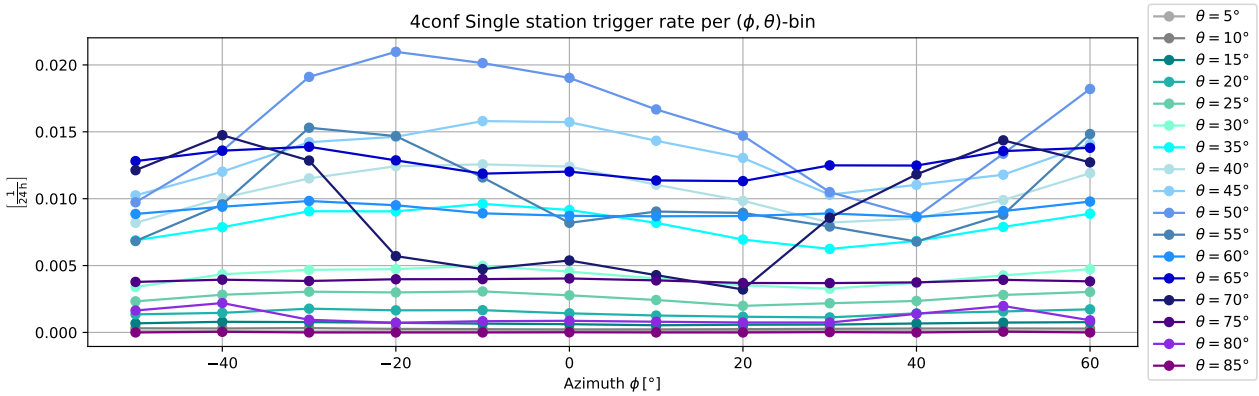

(b) Single station trigger rate for 4 antenna configuration, in every zenith and azimuth bin, $X_{(4\text{conf})}(\theta, \phi)$ from equation 5.16, as a series in θ of funcions of ϕ, in units of $\left[\frac{1}{24\,\text{h}}\right]$.

Figure 30

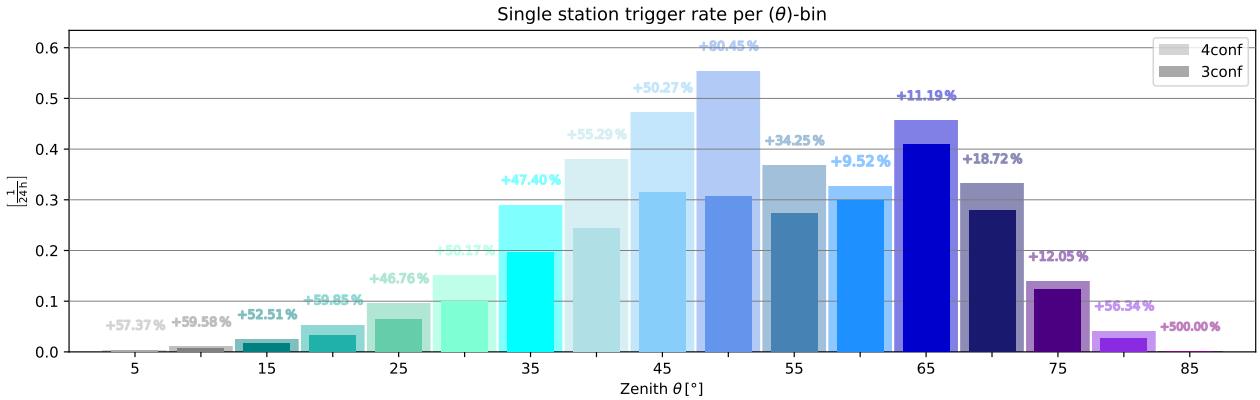

(c) Single station trigger rate in every zenith bin, by summation $\sum_\phi X(\theta, \phi)$ of all azimuth bins, according to equation 5.9, in units of $\left[\frac{1}{24\,\mathrm{h}}\right]$. The solid bars show the results for $X_{(3\mathrm{conf})}(\theta)$, while the translucent bars show $X_{(4\mathrm{conf})}(\theta)$. Trigger rates climb from the low and the high zenith range towards the peaks at $\theta = 45\,\mathrm{deg}$ and at $\theta = 65\,\mathrm{deg}$. The relative difference $\frac{X_{(4\mathrm{conf})}(\theta)}{X_{(3\mathrm{conf})}(\theta)} - 1$ is written above the respective bars. $X_{(4\mathrm{conf})}(\theta)$ performs 46-80% better in the low to mid zenith range $\theta \in [5, 50]\,\mathrm{deg}$, and 9-18% better for the higher zeniths $\theta \in [60, 75]\,\mathrm{deg}$.

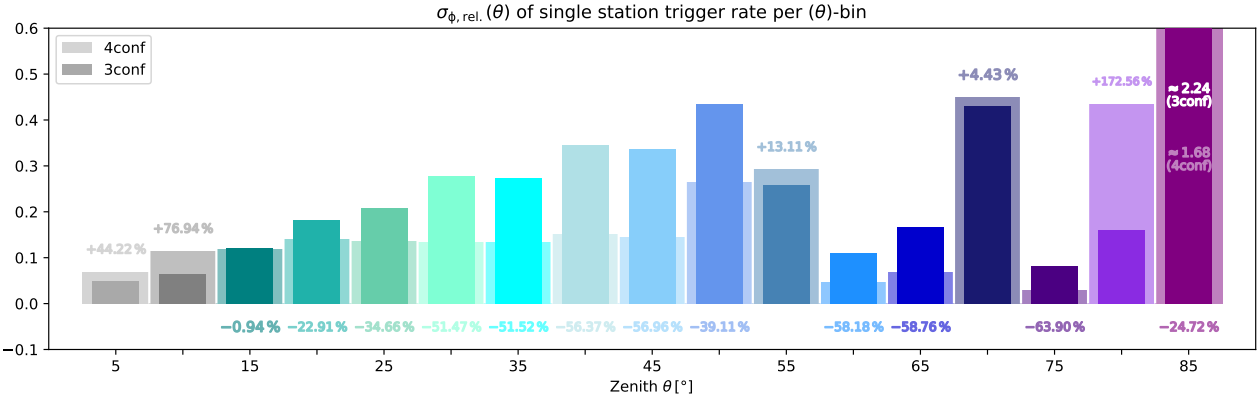

(d) Relative deviation of $X(\theta, \phi)$ with azimuth in every zenith bin, as calculated in equation 5.17. The solid bars show the results for $\sigma^{\mathrm{rel.}}_{\phi,\,(3\mathrm{conf})}(\theta)$, while the translucent bars show $\sigma^{\mathrm{rel.}}_{\phi,\,(4\mathrm{conf})}(\theta)$. The deviaton peaks for both configurations at the bins behind the peaks of their trigger rates, and has its greatest increase for $\theta > 80$ deg. At $\theta = 85$ deg it exceeds the other values in scale, so the graph was cropped for a better visulalization of the results. In the mid to high zenith range, it is optimal for both at $\theta = 60$ deg and $\theta = 75$ deg. The relative difference $\frac{\sigma^{\mathrm{rel.}}_{\phi,\,(4\mathrm{conf})}(\theta)}{\sigma^{\mathrm{rel.}}_{\phi,\,(3\mathrm{conf})}(\theta)} - 1$ is written above, if bigger, or below, if smaller, the respective bars. In most bins the 4 antenna configuration has the smaller deviation.

Figure 30: Analysis for every simulated zenith trajectory of single station trigger rate $X(\theta, \phi)$ as a function of azimuth.

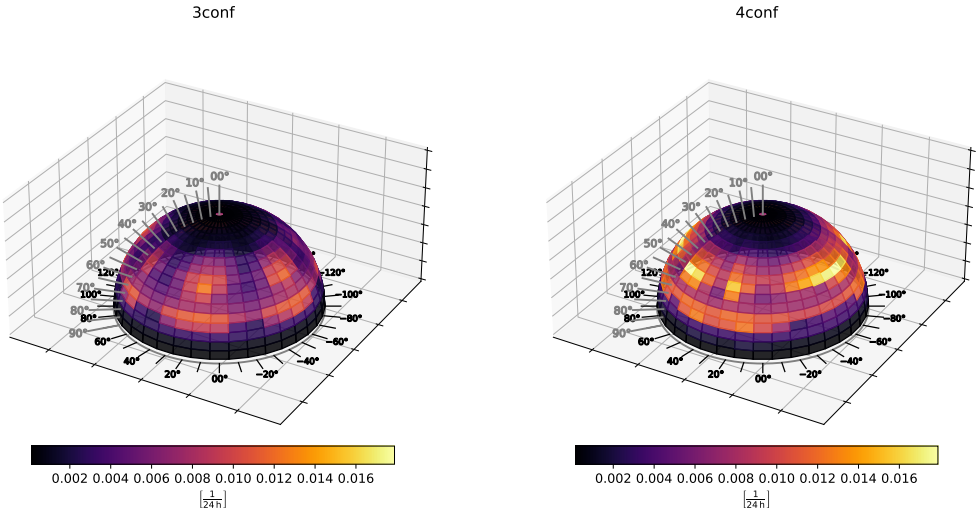

Figure 31: Visualization of single station trigger tate as a function of zenith and azimuth, according to equation 5.17 in units of $\left[\frac{1}{24\,\mathrm{h}}\right]$. Left: $X_{(3\mathrm{conf})}(\theta, \phi)$. Right: $X_{(4\mathrm{conf})}(\theta, \phi)$. The periodicy in azimuth is longer for $X_{(4\mathrm{conf})}(\theta, \phi)$, and it reaches higher trigger rates in most bins. The low zenith range has low trigger rates for both.

5.5 Analysis of trigger rate as a function of energy and zenith

When looking at the behaviour of the trigger rate in every energy and zenith bin as it is shown in figure 32 and figure 33, it becomes clear that at greater energies a higher zenith is maximum effective, and beyond that zenith the trigger rate drops very steeply. This is because the projected area of the footprint grows much faster with zenith, than the strength of the geomagnetic emission does. In very simplified terms, as the zenith increases, a stronger radio pulse will be spread over a much larger footprint, leading to an overall lower energy density, as can be seen from figure 9. At greater primary energies, a greater shower energy can be spread over a larger area before the energy density of the shower front drops below a critical density and becomes too weak to invoke a signal response strong enough to meet the threshold criteria.

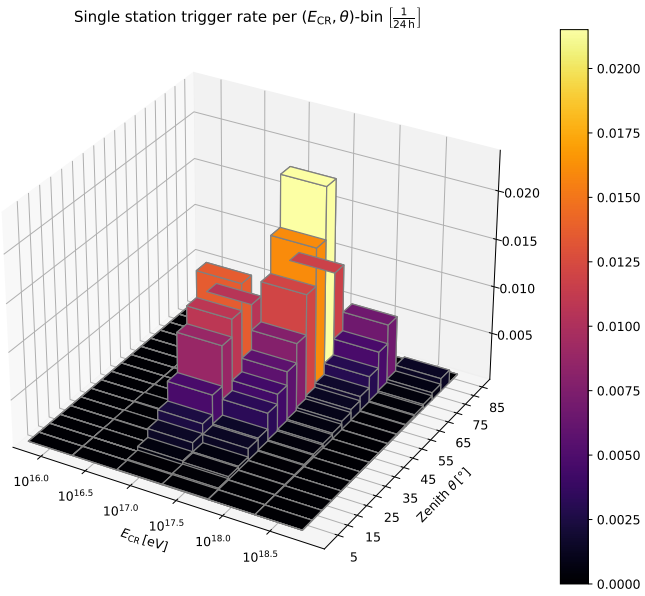

(a) Single station trigger rate of every energy and zenith bin for 3 antenna configuration, $X_{(3\text{conf})}(E, \theta)$, in units of $\left[\frac{1}{24\,\text{h}}\right]$.

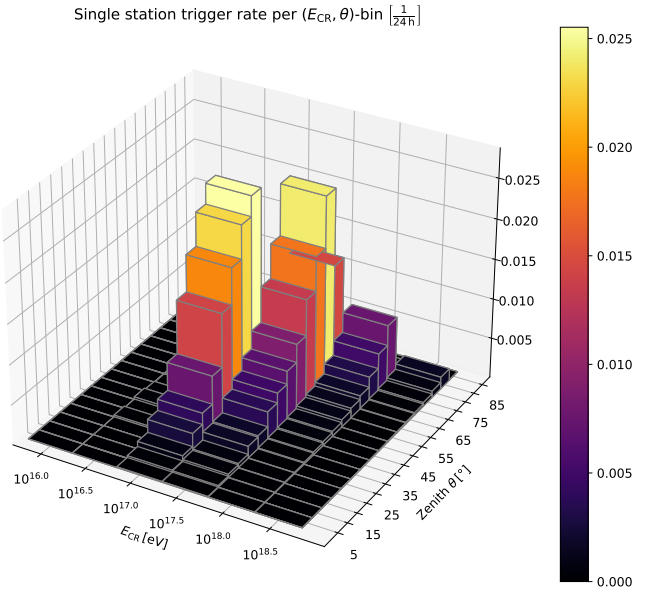

(b) Single station trigger rate of every energy and zenith bin for 4 antenna configuration, $X_{(4\text{conf})}(E, \theta)$, in units of $\left[\frac{1}{24\,\text{h}}\right]$. Please note the different scaling in comparison to figure 32a.

Figure 32

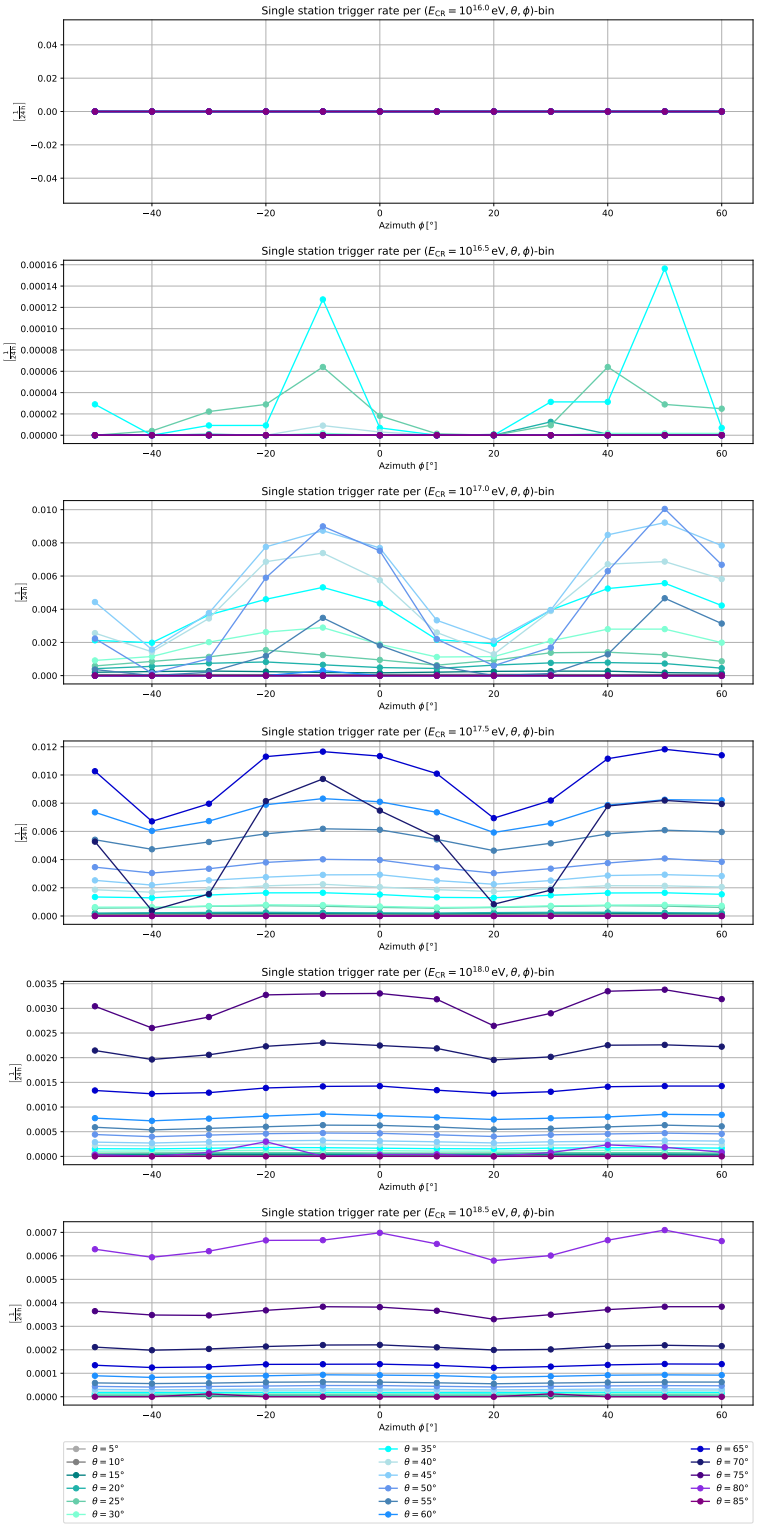

(a) Single station trigger rate in every energy, zenith and azimuth bin for 3 antenna configuration, $X_{(3\text{conf})}(E, \theta, \phi)$, in units of $\left[\frac{1}{24\,\text{h}}\right]$.

Figure 33

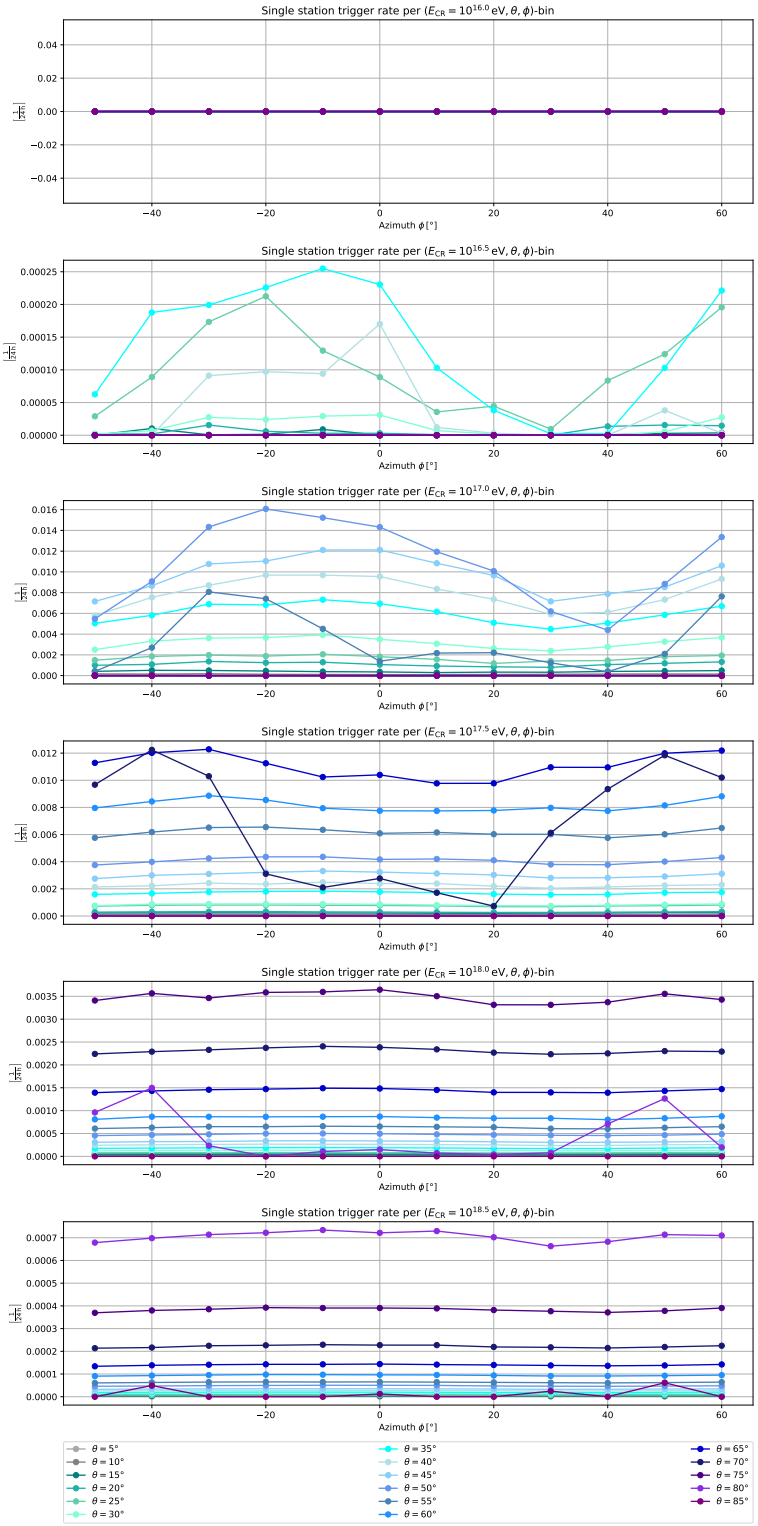

(b) Single station trigger rate in every energy, zenith and azimuth bin for 4 antenna configuration, $X_{(4\text{conf})}(E, \theta, \phi)$, in units of $\left[\frac{1}{24\,\text{h}}\right]$.

Figure 33

6 Conclusions

Through extensive simulations based on the hardware responses of detector layouts conducted with the NuRadioReco module [8], using the simulation files of radio pulses induced by extensive air showers, that were generated with the Monte Carlo approach based CORSIKA software [9] and the implemented endpoint formalism of the CoREAS extension [10], a clear result was deliverd on the original question of this thesis. It has been conclusively demonstrated, that the trigger efficiency offered by a triangular surface antenna configuration is outperformed by a quadratic antenna configuration in every aspect. When studying the trigger rate of both trigger configurations as a function of energy and azimuth in section 5.3, it became clear that the 4 antenna configuration yields higher trigger rates at every energy level, especially towards the lower end of the simulated energy range. Moreover, regardless of shower energy, its detection rates are more consistent and less subject to deviation with arrival azimuth, as the relative deviation with azimuth is at least 25 % smaller at every energy level.
From analyzing the trigger rates as functions of zenith and azimuth in section 5.4, as well as from graphic considerations of depicting the trigger rate as a series of functions of energy, zenith and azimuth, the 4 antenna trigger performed better in efficiency and consistency over the entire range of each single parameter, as well as over the entire span of every combination of these paramters. The consistent trend revealed from the graphic considerations is the behaviour of the blindspots, as they are clearly developed in every figure in chapter 5 that shows the trigger rate as a function of azimuth. While the 4 antenna array has a low in detectional sensitivity with a periodicy of 90 deg in azimuth, which equals 4 blindspots in 360 deg, the performance drops of the 3 antenna trigger rate are usually significantly greater and have a periodicy of 60 deg in azimuth, resulting in a total of 6 blindspots. The quantitative measures obtained in section 5.2, give the expected performance difference for the trigger rate of the quadratic surface array at 37.0 % better than the trigger rate of the triangular surface array, as well as the relative deviation with azimuth at a 53.0 % smaller. Therefore, based on these results, starting 2025 the RNO-G stations will be constucted using a quadratic surface antenna layout. The analysis of the geometry in section 4.3 showed that the differences in strength and

polarization of the geomagnetic emission differ quite strong at low zeniths, but since the low zenith contribution only make up 8.3 % and 9.1 % of the total trigger rate, respectively for 3 and 4 antenna configuration, the tendencies observed for the trigger rate summed over zenith are expected to differ very little from realistic conditions. However, considering the contribution of the askaryan emission, and the influence of the cherenkov compression on the footprint of the radio pulse, for a precise quantitative estimation of the expected number of daily trigger events, a more extensive set of air showers would have to be simulated.

Bibliography

[1] In: (). URL: https://ecap.nat.fau.de/index.php/research/neutrino-astronomy/radio-detection/.

[2] In: (). URL: https://rno-g.github.io/station-map/.

[3] J. Aguilar, P. Allison, J. Beatty, H. Bernhoff, D. Besson, N. Bingefors, O. Botner, S. Buitink, K. Carter, B. Clark, A. Connolly, P. Dasgupta, S. de Kockere, K. de Vries, C. Deaconu, M. DuVernois, N. Feigl, D. García-Fernández, C. Glaser, A. Hallgren, S. Hallmann, J. Hanson, B. Hendricks, B. Hokanson-Fasig, C. Hornhuber, K. Hughes, A. Karle, J. Kelley, S. Klein, R. Krebs, R. Lahmann, M. Magnuson, T. Meures, Z. Meyers, A. Nelles, A. Novikov, E. Oberla, B. Oeyen, H. Pandya, I. Plaisier, L. Pyras, D. Ryckbosch, O. Scholten, D. Seckel, D. Smith, D. Southall, J. Torres, S. Toscano, D. Van Den Broeck, N. van Eijndhoven, A. Vieregg, C. Welling, S. Wissel, R. Young, and A. Zink. "Design and sensitivity of the Radio Neutrino Observatory in Greenland (RNO-G)". In: *Journal of Instrumentation* 16.03 (2021), P03025. DOI: 10.1088/1748-0221/16/03/p03025. URL: http://dx.doi.org/10.1088/1748-0221/16/03/P03025.

[4] G. A. Askar'yan. "Coherent Radio Emission from Cosmic Showers in Air and in Dense Media". In: *Soviet Journal of Experimental and Theoretical Physics* 21 (1965), p. 658.

[5] M. Bleicher, E. Zabrodin, C. Spieles, S. A. Bass, C. Ernst, S. Soff, L. Bravina, M. Belkacem, H. Weber, H. Stöcker, and W. Greiner. "Relativistic hadron-hadron collisions in the ultra-relativistic quantum molecular dynamics model". In: *Journal of Physics G: Nuclear and Particle Physics* 25.9 (1999), p. 1859. DOI: 10.1088/0954-3899/25/9/308. URL: https://dx.doi.org/10.1088/0954-3899/25/9/308.

[6] T. P. A. Collaboration et al. *The Pierre Auger Observatory: Contributions to the 36th International Cosmic Ray Conference (ICRC 2019)*. 2019. arXiv: 1909.09073 [astro-ph.HE].

[7] D. García-Fernández, A. Nelles, and C. Glaser. "Signatures of secondary leptons in radio-neutrino detectors in ice". In: *Phys. Rev. D* 102 (8 2020), p. 083011. DOI: 10.1103/PhysRevD.102.083011. URL: https://link.aps.org/doi/10.1103/PhysRevD.102.083011.

[8] C. Glaser, A. Nelles, I. Plaisier, C. Welling, S. W. Barwick, D. García-Fernández, G. Gaswint, R. Lahmann, and C. Persichilli. "NuRadioReco: a reconstruction framework for radio neutrino detectors". In: *The European Physical Journal C* 79.6 (2019). DOI: 10.1140/epjc/s10052-019-6971-5. URL: http://dx.doi.org/10.1140/epjc/s10052-019-6971-5.

[9] D. Heck et al. "CORSIKA: A Monte Carlo code to simulate extensive air showers". In: (1998).

[10] T. Huege, M. Ludwig, and C. W. James. "Simulating radio emission from air showers with CoREAS". In: *AIP Conference Proceedings* 1535.1 (2013), pp. 128–132. DOI: 10.1063/1.4807534. eprint: https://pubs.aip.org/aip/acp/article-pdf/1535/1/128/11832917/128_1_online.pdf. URL: https://doi.org/10.1063/1.4807534.

[11] T. Huege, C. James, H. Falcke, and M. Ludwig. "The endpoint formalism for the calculation of electromagnetic radiation and its applications in astroparticle physics". In: *Proceedings of the 32nd International Cosmic Ray Conference, ICRC 2011* 4 (2011). DOI: 10.7529/ICRC2011/V04/0653.

[12] F. D. Kahn and I. Lerche. "Radiation from Cosmic Ray Air Showers". In: *Proceedings of the Royal Society of London Series A* 289.1417 (1966), pp. 206–213. DOI: 10.1098/rspa.1966.0007.

[13] K. Mase. "The latest IceCube results". In: *Nuclear Instruments and Methods in Physics Research Section A: Accelerators, Spectrometers, Detectors and Associated Equipment* 766 (2014). RICH2013 Proceedings of the Eighth International Workshop on Ring Imaging Cherenkov Detectors Shonan, Kanagawa, Japan, December 2-6, 2013, pp. 43–47. DOI: https://doi.org/10.1016/j.nima.2014.05.015. URL: https://www.sciencedirect.com/science/article/pii/S0168900214005142.

[14] S. Ostapchenko. "Monte Carlo treatment of hadronic interactions in enhanced Pomeron scheme: QGSJET-II model". In: *Phys. Rev. D* 83 (1 2011), p. 014018. DOI: 10.1103/PhysRevD.83.014018. URL: https://link.aps.org/doi/10.1103/PhysRevD.83.014018.

[15] L. M. Pyras. *Optimizing the triggering strategy for the detection of cosmic rays with the Radio Neutrino Observatory Greenland (RNO-G)*. 2020. URL: https://bib-pubdb1.desy.de/record/456326/files/Pyras_Msc.pdf?version=1.

[16] RNO-G et al. "Status and recent results from the Radio Neutrino Observatory in Greenland (RNO-G)". In: *PoS* ICRC2023 (2023), p. 1043. DOI: 10.22323/1.444.1043.

[17] O. Scholten, K. Werner, and F. Rusydi. "A macroscopic description of coherent geomagnetic radiation from cosmic-ray air showers". In: *Astroparticle Physics* 29.2 (2008), pp. 94–103. DOI: https://doi.org/10.1016/j.astropartphys.2007.11.012. URL: https://www.sciencedirect.com/science/article/pii/S0927650507001703.

[18] F. G. Schröder. "Status of the radio technique for cosmic-ray induced air showers". In: *Nuclear and Particle Physics Proceedings* 279-281 (2016). Proceedings of the 9th Cosmic Ray International Seminar, pp. 190–197. DOI: https://doi.org/10.1016/j.nuclphysbps.2016.10.027. URL: https://www.sciencedirect.com/science/article/pii/S2405601416302085.

[19] F. G. Schröder. "Radio detection of cosmic-ray air showers and high-energy neutrinos". In: *Progress in Particle and Nuclear Physics* 93 (2017), pp. 1–68. DOI: https://doi.org/10.1016/j.ppnp.2016.12.002. URL: https://www.sciencedirect.com/science/article/pii/S0146641016300758.

Declaration of authorship

I confirm that I have written this thesis unaided and without using sources other than those listed and that this thesis has never been submitted to another examination authority and accepted as part of an examination achievement, neither in this form nor in a similar form. All content that was taken from a third party either verbatim or in substance has been acknowledged as such.

Erlangen, 08.01.2024 Robin Valk

Acknowledgements

This thesis would not have been possible, without the support of the following people.

To my tutor at ECAP: Sjoerd, thank you for taking the time to answer all my questions. I know, there were a lot of them.

To my mum, thank you for bringing me food when I spend the entire day behind my desk and forget to take care of myself.

To my girlfriend, thank you for all the patience, all the kindness and all the motivating words. Thank you for always being in my corner. And thank you for keeping me from panicking, occasionally.